THE DEVELOPMENT OF A MICRO-NRA SETUP FOR BORON ANALYSIS

Matome Daniel Mookodi

A dissertation submitted in partial fulfillment of the requirements for the degree of Master of Science in Applied Radiation Science and Technology at North West University, Mafikeng

Supervisor: Dr W. Przybylowicz
August
2006

Declaration:

I hereby declare that the work contained in this dissertation is my own and has not been submitted for a degree or other degree or other qualification in other university or institution.

..... Date 24 August 2006

Matome Daniel Mookodi

ACKNOWLEDGEMENTS

I would like to thank the following people for their input in making this study a success.

Dr W. Przybylowicz, my mentor, for the guidance and support in preparation of this dissertation.

The Material Group Research Group staff; Dr C. Theron, Ion Beam Analysts; Mr. G. Pitsoane and Mr. P. Sechogela, van de Graaf Accelerator technicians; Mr Springhorn, Mr Doyle and Mr Marsh.

Dr G. Stevens and Esmé Spicer at the Geology Department, University Stellenbosch for assistance in sample preparation and analyses.

My family, who stood the pain of not seeing me regularly and whose prayers and support, were felt from a distance. To my friend Gabi, relatives and all the mates I've made as I moved from place to place. Onalenna, I never thought there are still some people who adhere to ubuntu principles, thanks adopted sister.

The iThemba LABS research institution for all the funds and equipment needed to carry out this study.

The CARST department, North West University for affording me the opportunity to study in this glorious field.

To Nquma Nonini, you have been supportive, willing to listen and your courage has rubbed off on me, and your constructive criticism is always welcomed.

To the Almighty, I know that my Mom says I don't praise you enough but deep inside me you are listening to all my silent prayers.

LE FA KELE MO MO GOROGORONG WA MORUTI WA LOSO, GA NKITLA KE TLHOKA SEPE KA ONA LENNA KA MATSATSI OTLHE

ABSTRACT

Matome Daniel Mookodi
iThemba Labs, Material Research Group, P. O. Box 722, Somerset West, 7129

Microanalysis of very low quantities of boron is required for various studies in geology and material science. This (analysis) was done at the nuclear microprobe chamber of Material Research Group in iThemba LABS. Since the solid angle of the annular Surface Barrier Detector is smaller and its position relative to the sample relatively far, the boron statistics are not optimal as will be seen in the study. Therefore an analytical set-up consisting of four large area PIN detector photodiodes was developed. Experimentally, the nuclear reaction $^{11}B(p, \alpha_1)^8Be$ showed to be free of interferences and gives good detection limits. The nuclear reaction gives a broad spectrum at E_p of 675 keV. The problem of backscattered protons was overcome by selecting a cut-off area where it is expected that the resultant alpha particles showing the presence of boron will be emanating.

The standards were Boron Nitride, NIST, tourmaline and glasses. The glasses were prepared by first making a matrix base material thereafter infuse boron as Boron Oxide. The samples were then analyzed using SEM/EDS techniques to acquire elemental abundances using EMP which proved to be not conclusive as a lot of problems were observed. That's due to the fact that final obtained values didn't correspond to the initial calculated values. The acquired SEM images were used though positively as they help in positioning of the glasses during experiments during both EMP and NMP.

The lowest obtained minimum detection limit was of a NIST 614 standard at 1.3μg/g for 0.303μC accumulated charge. The linear trend formed in the absence of the glasses gave a perfect agreement which meant that there were some discrepancies with them.

Contents

Chapter 1

1.1 Introduction.....1

1.2 Thesis composition.....3

Chapter 2

2.1 General Theory.....4
2.1.1 Ion Beam Analysis

2.2 Kinematical relations.....5

2.3 Scattering cross-sections and minimum detection limits.....5

2.4 Energy loss and stopping cross section.....8
2.4.1 Straggling
2.4.2 Nuclear stopping cross-section
2.4.3 Hydrogen stopping powers

2.5 Analytical Techniques.....12
2.5.1 Optical microscopy
2.5.2 Nuclear Reaction Analysis
2.5.2(a) NRA with charged particle detection
2.5.2(b) NRA with neutron detection
2.5.2(c) Particle induced gamma-ray emission
2.5.2.1 NRA principles and geometry
2.5.2.2 Q-value and Kinetic Energies
2.5.2.3 Resonance method

2.6 Scanning Transmission Ion Microscopy.....21

2.7 Particle Induced X-ray Emission.....23
2.7.1 X-ray production processes
2.7.1.1 Characteristic X-rays
2.7.1.2 Continuum X-rays
2.7.2 X-ray Spectroscopy
2.7.2.1 Pile ups

2.8 Rutherford Backscattering.....25
2.8.1 Kinematic factor

2.9 Secondary Ion Mass Spectrometry.....28
2.9.1 (a) Static SIMS

2.9.1 (b) Dynamic SIMS
2.9.1 (c) Depth profiling

2.10 Scanning Electron Microscopy.....30
2.10.1 (a) SEM operations
2.10.1 (b) Sample preparation

2.11 Historical Background Review.....33

Chapter 3

3.1 Experimental techniques and equipment.....36
3.1.1 Standards
3.1.1.1 Sample preparation
3.1.1.2 NIST standards

3.2.1 LEO EDS-SEM procedure.....37

3.2.2 LEO SEM Variable Pressure Procedure.....38

3.3.1 Nuclear microprobe.....38
3.3.1.1(a) On-demand beam deflection system
3.3.1.1(b) Beam instabilities
3.3.1.1(c) Data acquisition and analysis

Chapter 4

4.1 Results and discussion.....48
4.1.1 SEM and EDS
4.1.1.1 Elemental abundances

4.2 PIN Photodiodes Calibration.....55

4.3 NRA results using annular-Surface Barrier Detector.....60

4.4 NRA results using PIN photodiodes with Al foil.....68

4.5 NRA results using PIN photodiodes without absorber.....69

Chapter 5

5.1 Summary.....81

5.2 Conclusions.....82

5.3 Recommendations.....83

CHAPTER 1

BACKGROUND AND SCOPE OF INVESTIGATION

1.1 Introduction

Light elements as all natural elements are found in most of the earth's atmosphere and crust. Boron is a widespread constituent, being found in sedimentary, volcanic, plutonic and metamorphic environments albeit not very abundant element in the Earth's crust. The Earth's upper continental crust (average of 16 ppm B, 27th in abundance) is highly enriched in boron relative to the primitive mantle, which is inferred to have had 0.6 ppm B prior to the creation of the crust [Gre96]. It has shown to be a major component of geological materials due to its concentration in several rock-forming minerals. Due to its availability in different kinds of minerals, material scientists and geologists then noticed that a research was needed to analyze its characteristics, structure, properties and importance concerning the Earth's crust. The research interest spread when it was recognized that it is also applicable for nuclear and medical purposes. This has lead to various methods being applied to obtain as much information as possible regarding the use of boron in different disciplines mentioned above. This has lead to a breakthrough where it was found that boron has two naturally occurring isotopes: ^{10}B and ^{11}B with natural abundance of 19.9% and 80.1% respectively. Apart from these two, there are also synthetic, short-lived boron isotopes ranging in masses 7 to 9 and 12 to 16 [Gre96]. Important physical properties observed were melting and boiling points of values 2075^{0}C and 4000^{0}C respectively and also attained density range of 2.35 to 2.52 g/cm^3. The specific gravity of crystalline boron is 2.34 and of amorphous boron is 2.37. The element

with valence of +3 is a poor conductor at room temperature but good conductor at high temperatures.

The main aspect of every research is how one can benefit from attained information hence boron also does have an impact on modern environment. The element can be used as a compound to make borosilicate glasses, medical derivatives (Boron neutron capture therapy, arthritis treatment). Boron nitride, which is extremely hard, behaves as an electrical insulator yet conducts heat and has lubricating properties similar to graphite. Amorphous boron provides a green color in pyrotechnic devices. Boron-10 is used as a control for nuclear reactors to absorb neutrons and as a shield for nuclear reaction. Apart from the already mentioned research study cases, there has been an influx of studies on the element that lead to generated data based on geochemical, thermo chemical, mineralogical studies. Boron studies are relatively new because previously, analytical methods applied gave researchers problems hence less attention to it as compared to other light elements. Eventually the available data and research methods applied provides both an understanding of boron chemistry in geological environments and tools by which boron can be used to further our understanding of geological processes [Gre96].

The aim of this study was to develop locally at Material Research Group of iThemba LABS a technique of boron microanalysis at concentration as low as possible, based on nuclear reaction analysis. A new detector was used for this purpose, consisting of four positive intrinsic negative detector (PIN) diodes. Its performance was compared with the routinely used annular surface barrier detector (SBD). The initial part involved obtaining boron compounds and calibrating both detectors. Then the boron compounds were bombarded with proton beam and detected α-particles were read as boron events

depending on the energy. This was based on the Nuclear Reaction Analysis (NRA) equation, $^{11}B(p,\alpha)^{8}Be^{*}$, whereby an incident H^{+} of 660 keV interacts with ^{11}B and 3α-particles are detected after $^{8}Be^{*}$ decay. The majority of the experiment will be done at Material Research Group, iThemba Labs, Faure, South Africa though some of the measurements will be done at the Stellenbosch University, department of Geological Sciences. The measurements at Stellenbosch University included SEM and EDS to help in the location of boron oxides in different glasses and the determination of concentration of matrix elements and boron respectively.

The new detector was mounted in the experimental chamber of the nuclear microprobe. Though NRA was the main method of boron determination in the study, Scanning Electron Microscopy and Optical microscopy were used for comparison between EMP and NMP and locating of B_2O_3 glasses in the resin respectively.

1.2 Thesis composition

The whole write-up consists of chapter 1 with background, scope of investigation and objectives. Chapter 2 has introduction to types of analytical techniques, description of nuclear microprobe and accelerator and general theory. Chapter 3 comprises the details of experimental equipment and techniques. Chapter 4 constitutes data analysis and results. Chapter 5 contains summary, calculations, recommendations and conclusion

CHAPTER 2

2.1 General Theory

2.1.1 Ion Beam Analysis

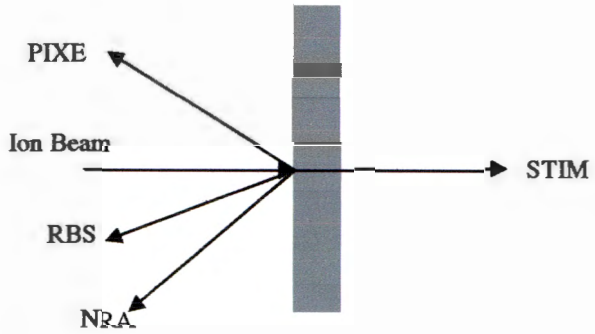

Fig 2.1 Types of ion beam techniques possible at the iThemba Labs NMP [www10]

When a charged particle moving at high speed strikes a target, the projectile slows down and possibly deviates from its initial trajectory. This can lead to emission of particles or radiation whose energy is characteristic of the elements which constitute sample material [www2]. A common scenario in all of the analysis techniques is that during ion beam – target interactions, most of the individual particles penetrate specimen in roughly their incident direction gradually losing energy until they stop close to their ultimate range in that particular matrix. It's only a certain type of particles that will get as close as possible to the nucleus of the target, normally neutrons (uncharged particles), as their stopping power has a longer range. The stopping power, (dE/dx), is the loss of energy and is described in terms of energy loss per unit thickness of material traversed, keV (mg. cm^{-2})$^{-1}$. Stopping power depends on the type of an ion, its energy and the matrix composition [Wat87].

Different kinds of analysis (eg NRA in this study) are employed to acquire information about the composition of biological, metallurgical, medicinal, etc samples and all this depend on the type of analytical technique employed.

2.2 Kinematical relations

In atomic and nuclear collisions two systems of reference are used: Laboratory and centre-of-mass (c.m.) systems.

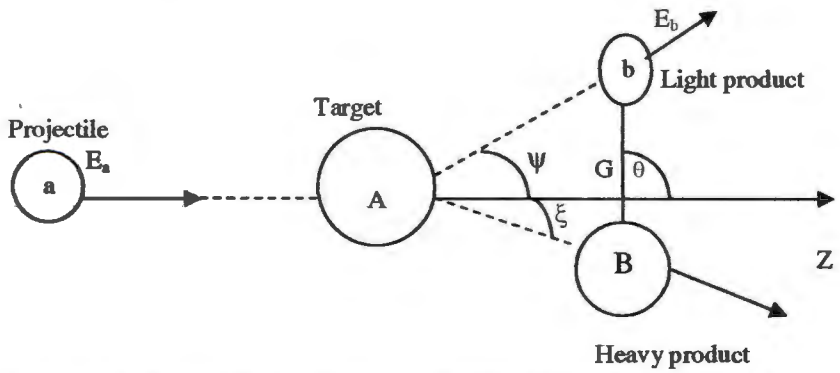

Fig 2.2 Laboratory and centre-of-mass reference coordinate systems [Dec78]

From figure 2.2 description of the laboratory frame of reference is detailed. The incident ion a with mass m_a bombards target A of mass m_A and products b and B of masses m_b and m_B are emitted at angles ψ and ξ respectively. Supposing $m_b < m_B$, B is named a heavy product. The centre-of- mass system is the frame of reference in which the interaction is most simply described. The starting point of coordinate is the centre-of-mass G of the colliding particles. Particle b is emitted at angle θ and B at an angle $(\pi - \theta)$ with respect to the incident particle direction. The incident particle energy is mostly given in the laboratory system and the angular coordinates in the centre-of-mass system.

2.3 Scattering Cross-sections and Minimum Detection Limits

The interaction of the projectile and its target is depending on the availability of an element itself in the matrix. That is determined by the magnitude of the cross-section which a target

atom has for producing detected signal. This detected signal is captured by the detector corresponds to (though not all products are detected) the magnitude of the cross-section. The idea of how frequent is the projectile/target interaction occurring, is taken from a simple conceptual experiment where a narrow beam of fast particles impinges on a thin uniform target that is wider than the beam. At an angle θ from the incidence direction, let an ideal detector count each particle scattered in the differential solid angle dΩ. If Q is the total number of projectiles hitting the sample and dQ is the products detected, then the differential scattering cross section, dσ/dΩ, is given by

$$\frac{d\sigma}{d\Omega} = \left(\frac{1}{Nt}\right)\left[\left(\frac{d\sigma/d\Omega}{Q}\right)\right] \quad \text{.....Eq 2.6}$$

where

- N is the volume density of atoms in the target
- t is the target's thickness
- Thus Nt is the number of target atoms per unit area (areal density) [Chu78]

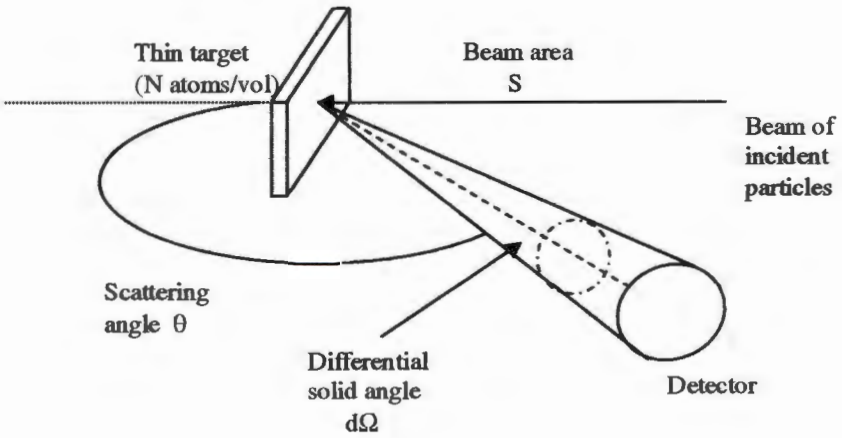

Fig 2.3 Experimental layout demonstrating the concept of differential scattering cross section. [Chu78]

From the schematic drawing above, fig.2.3, it shows that only projectiles that are scattered within the solid angle dΩ spanned by the detector are counted. This shows that although the solid angle is small, the scattering angle is well defined [Chu78]. The definition of the equation assumes that the thickness, t, is minimal hence energy loss of the particles in the target is so small that the energy of the incident particles is virtually the same at any depth of the target. It also assumes that the total number of projectiles, Q, must be so large that the ratio dQ/Q has a well-determined value.

The cross-section that can be written as $d\sigma/d\Omega$, is named in units barns per steradians ($1barn = 10^{-24}cm^2$) [Wat87]. This is because the probability of reaction between a projectile and a target nucleus can be approximated by the geometrical cross section given by the target nucleus to a point-size incident ion. The nuclear radius is given by the formula

$$R = R_0 A^{\frac{1}{3}} \quad \text{.....Eq 2.7}$$

where

- A is the mass number
- R_0 is a constant (1.4×10^{-13} cm)

To calculate the geometrical cross section

$$\sigma_{geo} = \pi(R_0 \times A)^2 \quad \text{.....Eq 2.8}$$

From the above equation, obtained cross-section values are in the order of $10^{-24}cm^2$ hence the unit barn. From the cross section depending on its size, the element's concentration can be analyzed from the whole matrix. This is done by expressing it (concentration) as a percentage or in parts per million (ppm) of the total matrix. Since there is no certainty about the form of the concentration, in terms of weight (w) or number of atoms (a), notations are normally w%, wppm or a%, appm. The ability of the technique to detect

minimal concentrations of trace elements in a matrix is referred to as its sensitivity or minimum detectable limit (MDL). MDL is the trace element concentration (usually in wppm) that is needed to give

Counts in the peak = $3(N_{background})^{1/2}$ .....Eq 2.9

where

- N is the background counts under Full Width at Half Maximum (FWHM) of the peak.

MDL can also be attained by at least ten counts [Wat87]. The application of either is based on which is larger [Sko03]. MDL does depend on the experimental procedure such as duration of measurement and quality of detector though [Wat87].

2.4 Energy loss and stopping cross section

Knowing how the projectile slows down in transversing material is of importance in methods of material analysis using charged particles. Depth profiling and sensitivity specifically are proportional to the energy lost by the probing particles and the energy loss affects both quantitative and compositional analysis. Definitions of concepts energy loss, specific energy loss, stopping cross section and stopping power vary according to literature though they may have similar symbols.

Energy loss $\left(\frac{dE}{dx}\right)$: $\Delta E/\Delta x \rightarrow \left(\frac{dE}{dx}\right)$, when $\Delta x \rightarrow 0$, where ΔE is the amount of energy lost per distance traversed. dE/dx is also known as the stopping power or specific stopping power and energy loss is denoted by ΔE [Tes95].

Stopping cross section: $\varepsilon = \left(\frac{1}{N}\right)\left(\frac{dE}{dx}\right)$ or $\varepsilon = \left(\frac{1}{\rho}\right)\left(\frac{dE}{dx}\right)$ where N is the volume density and ρ is the mass density. ε is sometimes called stopping power [Tes95].

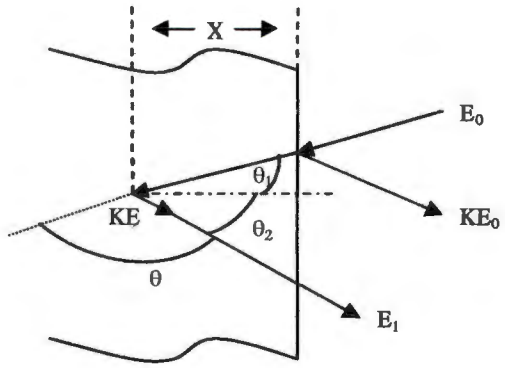

Fig 2.4 Description of backscattering events in a sample consisting of a monoisotopic element. [Chu78]

The diagram above shows energy E_1 of the detected particle after incident ion of energy E_0 has passed through a target of depth X of monoisotopic elemental sample. With the geometry above, we can relate E to the length $x/\cos\theta_1$ of the projectile path by

$$x/\cos\theta_1 = -\int_{E_0}^{E} dE/(dE/dx) \quad \text{.....Eq 2.10}$$

The negative sign shows that energy E, energy just before ion-target collision, is lesser than E_0. Path length $x/\cos\theta_2$ of the resultant particle path is related to KE and E_0 by

$$x/\cos\theta_2 = -\int_{KE}^{E_1} dE/(dE/dx) \quad \text{.....Eq 2.11}$$

If dE/dx is constant for both entrance and exit paths, equations 2.10 and 2.11 above lessen

to $$E = E_0 - \frac{x}{\cos\theta_1}\frac{dE}{dx}\Big|_{in} \quad \text{.....Eq 2.12}$$

and $$E_1 = KE - \frac{x}{\cos\theta_2}\frac{dE}{dx}\Big|_{out} \quad \text{.....Eq 2.13}$$

Eliminating E form the two equations yields

$$KE_0 - E_1 = \left[\frac{K}{\cos\theta_1}\frac{dE}{dx}\Big|_{in} + \frac{1}{\cos\theta_2}\frac{dE}{dx}\Big|_{out}\right]x \quad \text{.....Eq 2.14}$$

The energy change or difference $[S]x = KE_0 - E_1 = \left[\frac{K}{\cos\theta_1} \frac{dE}{dx}\Big|_{in} + \frac{1}{\cos\theta_2} \frac{dE}{dx}\Big|_{out} \right] x$ is called the energy loss factor [Chu78].

2.4.1 Straggling

Apart from energy loss resulting in beam slowing down, deviation can occur as the projectile transverses through the material. This results in spreading of the beam energy, a phenomenon called energy straggling. This is attributed to statistical fluctuations in collisions processes. Therefore identically particles with the same initial velocity end up with different final energy after passing through the target with homogeneous medium. Energy straggling in material analysis broadens energy distributions and resonances i.e gives a Gaussian distribution when energy loss results in final energy being less than incident one, and impairs depth and mass resolutions except for atoms on top of the surface [Tes95]. According to Bohr's theory, the energy straggling does not depend on the energy of the projectile and that the value of the energy variation increases with the square root of the electron density per unit area in the target. The cause of the above-mentioned disadvantages is because the beam after colliding with the target, it losses its initial monoenergetic character and hence the ratio of E_1/E_2 and M_2 identification are not certain. To compensate for these problems quantitative knowledge of parameters, projectile energy and mass, is vital [Chu78].

2.4.2 Nuclear stopping cross-section

Total stopping cross-section of ions is composed of two parts, related to the energy transferred by the ion to the target electrons (named electronic stopping or inelastic energy loss) and to the target nuclei (called nuclear stopping or elastic energy loss). In classical

two particle scattering non-relativistic elastic collisions, the following holds for laboratory co-ordinates:

Conservation of Energy: $E_0 = \frac{1}{2}M_1 v_0^2 = \frac{1}{2}M_1 v_1^2 + \frac{1}{2}M_2 v_2^2$ .....Eq 2.16

where

- E_o is the ion's initial kinetic energy
- v_o is the incident velocity of the ion with mass M_1
- v_1 is the ion's final velocity after striking target atom of mass M_2 ,which recoils with velocity v_2

Adding the above mentioned equation with the conservation of momentum equations, both longitudinal, $M_1 v_0 = M_1 v_1 \cos\vartheta + M_2 v_2 \cos\phi$,

and lateral, $0 = M_1 v_1 \sin\vartheta + M_2 v_2 \sin\phi$,

then eliminating the target recoil angle we obtain

$$\left(\frac{v_1}{v_0}\right)^2 - 2\left(\frac{v_1}{v_0}\right)\frac{M_1}{M_1 + M_2}\cos\vartheta - \frac{M_2 - M_1}{M_2 + M_1} = 0 \quad \text{.....Eq 2.17}$$

This equation with laboratory coordinates is related to the centre of mass coordinates equation via $T = \frac{2}{M_2}\left(v_0 M_c \sin\frac{\theta}{2}\right)^2 = \frac{4M_c M_c}{M_2}\sin^2\frac{\theta}{2} = \frac{4E_0 M_1 M_2}{(M_1 + M_2)^2}\sin^2\frac{\theta}{2}$ .....Eq 2.18

where

- T is the energy transferred from projectile to the target [Zie85].

The above relations give the stopping power of the projectile when we evaluate the energy loss cross-section because they contain the energy lost by the projectile.

2.4.3 Hydrogen stopping powers

Energy-loss of light positive ions, hydrogen and helium, is of large interest in basic and applied physics. Incident hydrogen beam has small nuclear stopping power for energies that are very low (~ 1-2 % at 10 keV and increasing in relative importance with decreasing energy) [And77]. At energies of between 600 – 2000 keV experimental data is largely scattered and less theoretical guidance can be obtained concerning the so-called shell corrections. To obtain easy high precision stopping cross sections, Bethe formula can be applied.

$$S = \frac{4\pi e^4 Z_1^{\,2} Z_2}{mv^2} \times \left[\ln\left(\frac{2mv^2}{I}\right) + \ln\left(\frac{1}{1-\beta^2}\right) - \beta^2 - \frac{C}{Z_2} \right] \quad \text{.....Eq 2.18}$$

where

- m is the electron mass and $\beta = v/c$
- c is the velocity of light
- I is the main parameter of the theory i.e mean excitation potential
- C/Z_2 is the shell corrections

Therefore it means the Bethe formula will not be applicable for energies below 600 keV [And77].

2.5 Analytical Techniques

Analytical techniques are classified by their types of incident beams hence the electron and nuclear microscopy. Nuclear microscopy is a method whereby a device called microprobe is used to focus an ion beam using electromagnetic lenses [www3]. Electron microscopy is a method similar to nuclear microscopy but the electron lenses are used to focus an electron beam in an electron microprobe device. This microscopy type is applied to image small

object which are difficult to obtain by light microscopy. An example is images obtained using energy dispersive spectrometry [www4]. The analysis as mentioned will be done using NRA but there are also possible energy sensitivity-profiling techniques. Though they (other techniques) are normally excellent in depth profiling, they can be used in sensitivity profiling because they have detection limits of ppm range or even ppb. This obtainable limit ranges help in trace elements detection of which includes boron. The problem with these trace elements is that they are not easy to detect due to the number of interfering elements because most of the time they are in compounds where a lot of heavier elements dominate. The proposed NRA method is a poor depth-profiler but this is no problem in this study because we are concerned with sensitivity. As mentioned, there are numerous techniques (Electron Microprobe included) that could be used but we only concern ourselves with the following in this study:

- Optical Microscopy
- Nuclear Reaction Analysis (NRA)
- Secondary Ion Mass Spectrometry (SIMS)
- Scanning Electron Microscopy (SEM)

2.5.1 Optical microscopy

The technique helps in screening structures that are very small in size, micrometer ranges, by enlarging them using electronic devices. An optical microscope makes use of lenses to bend light, hence image magnification. Most light microscopes can operate in either transmission or reflection mode. With our optical microscopy, Nikon LABOPHOT type 104 connected to a Sony video camera model SSC-DC 30 P, images can be viewed in the eyepieces or digitally captured on the computer. The microscope also has horizontal and

vertical controls with accuracy of the order of a micron, and has incident light source--a halogen lamp. The negative side is the contrast which is though good it's not sufficient to show the smoothness of the glasses. Therefore before any final decision is made on the position of the beam spot on the glasses, it would be advisable to take other pictures using SEM which is more reliable in showing the surface structure of materials [www1].

2.5.2 Nuclear Reaction Analysis

The occurrence of this technique depends on strong interaction of the incident beam with a target nucleus and resultant altered nucleus decays into detected products. This can only happen if the incident beam has enough energy to overcome the Coulomb barrier. The incident ion energy must be greater than

$$E = \frac{zZ}{[\sqrt[3]{a} + \sqrt[3]{A}]} \text{MeV} \quad \text{.....Eq 2.19}$$

where

- z and Z are atomic numbers of projectile and target nuclei respectively
- a and A are atomic weights of projectile and target nuclei respectively [Wat87]

Coulomb barrier heights vary with Z for light ions; however the loosely bound structures of deuteron, triton, ^{3}He nuclei make them interact at lower energies than what is presumed by the equation above. When a projectile succeeds in penetrating the Coulomb barrier of a target nucleus, the characteristic behavior of either a direct or a compound nucleus reaction is often seen. In a compound nucleus, i.e after interaction, the altered nucleus will either lose its internal energy by emitting gamma rays or break up into few particles. With that in mind, due to internal nuclear property change, the products normally will have a larger mass than reactants called Q-value and are reported in MeV units. When using low energy

incidents, only reactions with low Z will occur making NRA the best in picking low Z elements in high Z matrices.

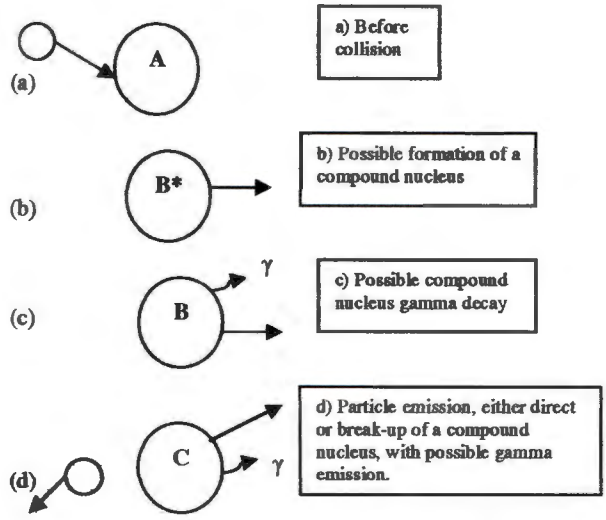

Fig 2.5 Illustration of different NRA reaction types. Smaller circles denote light particles and bigger ones heavier particles. The asterisk indicates an excited nucleus [Wat87]

The above illustrations show that NRA can have different types of decay modes during compound reaction occurrence. Though the situation in figure 2.5(d) is assumed to be direct or compound reaction process, the mechanism can indeed occur without projectile combining fully with the target. Though it doesn't occur frequently, NRA can be done using heavier products that offer beta decay with subsequent gamma emission. This can be good because of high sensitivities but reactions are not being used due to these products having longer half-lives than those of the main reactions [Wat87]. NRA can have different detected products such as charged particles, neutrons, gamma rays and sometimes beta decay prior to gamma rays.

2.5.2 (a) NRA with charged particle detection

An NRA measurement uses a beam of several nanoamps of 1 to 10 MeV light ions to generate MeV protons or α-particles as charged-particle reaction products from light

elements found in a matrix. This can be attained by performing NRA with microbeams capable of obtaining enough signals with a relatively small cross-section but decent level of sensitivity. The best is to have a detector with a solid angle of about 0.2sr with 100% efficiency [Wat87]. This large area semiconductor detector is normally covered with an absorber to stop backscattering ions from being measured, as this would degrade the analytical sensitivity. If the detected ions are from the reaction only and there is very little background in the measured spectrum, then sensitivities of 0.01ppm can be achieved under favorable conditions. Although the most popular incident ion have been deuteron which gives (d, p) with several important light elements, there has been a sudden burst of other projectiles such as H^+, ^3He, etc. This has enabled research on H^{2+} itself and other targets, which were not brilliantly profiled by deuteron. Nuclear reaction products have a problem with interferences as we notice in our focal reaction, $^{11}B(p,\alpha_1)^8Be^*$ where subsequent $^8Be^*$ decay leads to two extra α-particles whereas we are interested in the first one. To counter-act the problem, there must be concentration on the counts of specific energy which are assumed to be true, such as the broad resonance of the $^{11}B(p,\alpha_1)^8Be^*$ reaction where true counts are between 300 and 600 keV [Sko03].

Obtained yield from a charged particle induced reaction, unlike in RBS, has no analytical formula for cross-section. Generally high Z elements do not undergo nuclear reactions in MeV range due to Coulomb barrier repulsion and also because emitted particles have very high Q-values as compared to projectiles hence detection of background-free light elements on heavier substrates [Fel86]. The detected particles value is given by $Q_D = N_s\sigma(\theta)Q\Omega$ where

- Q_D is the detected particles number

- N_s is the total number of atoms/cm^2
- $\sigma(\theta)$ is the differential cross-section
- Q is the number of incident particles
- Ω is the detection solid angle

2.5.2 (b) NRA with neutron detection

Due to problems concerned with working with neutrons even as a projectile, there is not a lot about its detection. It is less convenient to use compared to charged particles as noticed by small number of available microbeam measurements. The appropriate neutron detector is a liquid scintillator with capability to discriminate against gamma rays. Unlike in charged particles spectra where a peak can be clearly seen, spectrum given by liquid scintillator shows a roughly rectangular shape from maximum depending on the neutron energy down to zero.

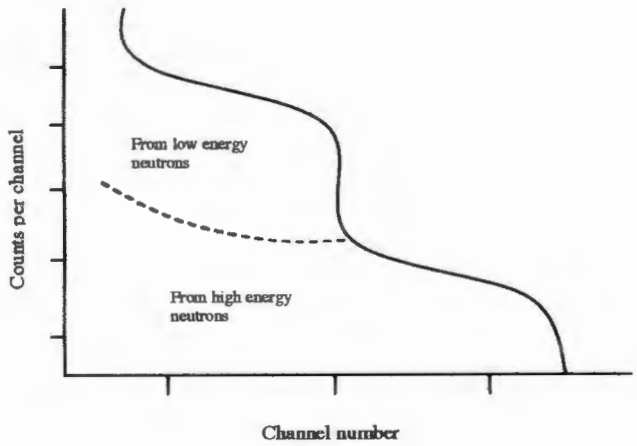

Fig 2.6 The type of spectrum produced in a liquid scintillator by neutrons of two different energies. [Wat87]

The above indicates that it will be very difficult to get true events of a certain elements because of lack of peaks. Due to lack of neutron energy resolution the only microbeam (charged-particle, neutron) analyses have involved reactions with high Q values.

2.5.2 (c) Particle Induced Gamma Emission

An example of NRA whereby gamma rays are detected as part of resultant products. Beams of different ions, protons, deuterons, tritons, ^{3}He, ^{4}He have been used to perform NRA with gamma ray detection. The advantage of this technique is its non-destructiveness and easy use of external beams when γ-ray detection is desired [Tro99]. For PIGE to occur there must strong interaction between element of interest and beam giving gamma rays that are free of interference of gamma rays of similar energy [Wat87]. The gamma rays can be prompt or delayed depending on the type of reaction and incident energy.

2.5.2.1 NRA principles and geometry

Nuclear reaction analysis is more suitable to perform analysis for light elements than Rutherford backscattering because, depending on the parameters, its cross section does not increase with the square of the atomic number [Bar99]. The evidence is seen when a light element is placed on a heavy substrate where the RBS spectrum of the same light element will appear on top of the heavy element's spectra. Though there is a significant difference of results, basically the same equipment is applicable for both techniques [Tes95]. The geometry of the NRA technique can be either forward or backwards and the scattering geometry is similar to that of RBS except that in NRA the filtering equipment is in front of the detector (see figure 2.7).

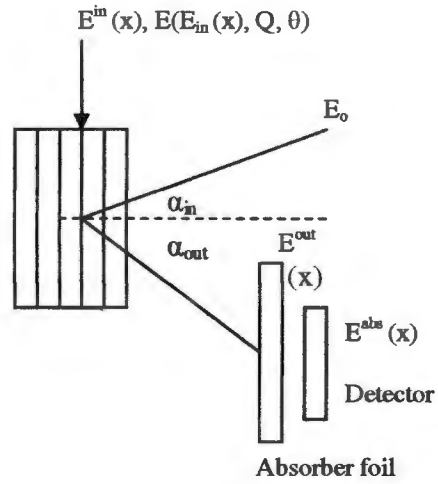

Fig 2.7 Characteristic NRA experiment geometry
[Tes95]

From the diagram above, the energy of the products leaving the target is given by

$$E_{out}(x) = E[E_{in}(x), Q, \Theta] - \int_0^{x/\cos\alpha_{out}} S_{out}(E)dx \quad \text{.....Eq 2.20}$$

$$E_{in}(x) = E_0 - \int_0^{x/\cos\alpha_{in}} S_{in}(E)dx \quad \text{.....Eq 2.21}$$

where

- x is the depth of the nuclear reaction location
- E_0 is the energy of the projectile
- Q is the Q-value of the reaction
- S(E) is the stopping power of the projectile and the out-going product
- α_{in} and α_{out} are angles of both projectile and detector relative to the surface normal of the sample surface
- $E[E_{in}(x),Q,\theta]$ is energy of the reaction products

- Θ is the scattering angle [Tes95]

There are about five kinds of filtering that can be applied [Tes95], but we will only concentrate on the foil technique as it will be used in this study as the backscattered protons barrier.

2.5.2.2 Q-value and Kinetic Energies

Nuclear reactions, like any reaction, obey laws of conservation be it nucleons, charge, mass-energy and momentum [Fel86]. The evidence is seen when comparing the total of reactants rest masses with those of the resultant products. The difference observed is due to the mass and energy exchange according to the law

$E = mc^2$ .....Eq 2.21

where

- E is the energy
- m is the mass
- c is the speed of light with 1 mass unit equal to 931.4 MeV

The Q-value can be negative or positive depending on whether the reaction is endoergic or exoergic respectively. A nuclear reaction which can systematically be written as

M_1 (projectile) + M_2 (target) $\longrightarrow$ M_3 (emitted radiation) + M_4 (residual nucleus) + Q

If the M's are taken to be masses, then Q is simply the difference between the masses

$Q = [M_1 + M_2]\, c^2 - [M_3 + M_4]\, c^2$

Q-value also can be used to determine the type of reaction, eg if M_3 is taken to be a gamma ray then a nuclear reaction is named direct capture reaction. The other conditions are when $M_1 = M_3$ and $Q = 0$ then elastic scattering reaction is observed.

$M_1 = M_3$ but Q-value $\neq 0$ then inelastic scattering reaction is obtained. Finally $M_1 \neq M_3$ means a rearrangement collision [Fel86].

2.5.2.3 Resonance method

Though our study will be based on a very broad resonance spectrum, there are times where a nuclear reaction does give a very narrow resonance and a peak. Such reactions like $^{11}B(p,\alpha_1)^8Be^*$ at E_p= 163 keV can be used in depth profiling of trace elements. In a situation where only one resonance existing in a cross-section curve is considered, gamma rays from projectile and impurity atoms interaction are measured as yield versus incident energy (Fel86). Slowing down incident energy E_0 until resonance energy E_R is reached at depth x, we get a nuclear reaction transpiring at a rate similar to the impurity concentration. Relation between depth x and E_0 is equation

$$E_0 = E_R + \left(\frac{dE}{dx}\right)_{in} \frac{x}{\cos\theta_1} \quad \text{.....Eq 2.22}$$

where

- θ_1 is the between incident beam and surface normal
- $\left(\frac{dE}{dx}\right)_{in}$ is the constant stopping power

By simply changing to depth and concentration scales from energy and yield respectively, one will be able to pick the concentration of the trace element but not from the surface as that will be contaminated [Fel86].

2.6 Scanning Transmission Ion Microscopy

STIM uses transmitted ion energies measured number of ions per pixel to generate an image showing areal density variations. The technique was developed to quantitatively image areal density distributions in thin biological samples, analyze in tandem with PIXE

or backscattering spectrometry and to normalize PIXE images [Bre96]. Biomedical researchers use STIM to image unstained cells subsequent to PIXE analysis thereby avoiding contamination of the samples by chemical dyes. The method relies on well defined energy loss of the ion caused by ion-electron interactions in a sample. With the Si detector placed at 0^0, behind the sample, energy loss of each ion is measured and if the scanning microbeam is on then energy loss transmission images can be formed [Joh95]. There is a large momentum difference between ion and electron hence a small scattering angle observed. The use of MeV beams in STIM means minimal spreading of the beam and subsequent imaging of fine details in relatively thick samples [Joh95]. But also a large number of collisions occur among MeV ions that lead to aberrations such as energy straggle, lateral and angular spread of the resultant beam at the rear of the sample.

Table 2.1 Comparison of different STIM analysis ions.[Bre96]

Sample	Ion	Energy (MeV)	r_e (nm)	dE/dZ (keV/μm)	Ω_B^2 (keV)	Range (μm)
Silicon	p	5.5	5.9	13	2.6	251
$\rho = 2.3 g/cm^3$	Li	6.0	6.3	356	6.1	14.5
	C	12.0	6.1	1046	8.2	10.8
Gold	p	3.0	32	714	8.3	27.0
$\rho = 19.3 g/cm^3$	p	5.5	22	502	9.9	67.3
	Li	6.0	34	1050	37	5.7
	C	12.0	35	3120	84	4.2

2.7 Particle Induced X-ray Emission

This is the most applied nuclear microscope technique of trace elements analysis mostly used for biological, geological, etc specimens. The MeV H^+ ion beam bombards a sample and X-rays are detected by a Si(Li) detector. The pulses from the detector will then be amplified and finally recorded in the pulse height analyzer. Each peak from the PIXE spectrum has a number of pulses, and is a barometer of the concentration of the corresponding element in the specimen. With known parameters, solid angle, x-ray production cross-sections, detector efficiency, etc it is possible to obtain absolute elemental concentration [Joh95].

2.7.1 X-ray production processes

MeV light ions and keV electrons have high cross-section for ejecting K, L or M shell electrons because their velocity approaches the inner shell electron velocity. Generation of different X-ray lines is caused by de-excitation of electrons from different shell levels. For an example, a vacancy in the K shell results in a K_α X-ray being emitted if an L shell electron fills the vacancy and a more energetic K_β X-ray is emitted if an M or N shell electron fills the vacancy. K_α X-ray emission is more probable than K_β X-ray emission though. L_α, L_β and L_γ X-rays emission are also caused by an L shell vacancy being filled by an electron transition from a higher shell. To get excellent trace element profile quantification using PIXE, one needs accurate knowledge of electron-shell ionization cross-sections [Bre96].

2.7.1.1 Characteristic X-rays

Production of characteristic X-rays by an element is dependent on the deexcitation of vacancies produced by ionization through Coulomb interaction of charged beam particles with inner shell electrons [Joh95].

2.7.1.2 Continuum X-rays

The sensitivity of each technique is limited by the amount of background underlying the characteristic X-rays. In PIXE there are a number of background sources, like the initial braking radiation from scattering from nuclei in the target, electron bremsstrahlung and gamma rays from nuclear reaction. [Wat87 and Joh95]. Unlike in characteristic X-rays lines, projectile bremsstrahlung due to protons is much less than that induced by electron beams. The intensity of the projectile bremsstrahlung is proportional to its deceleration.

2.7.2 X-ray Spectroscopy

2.7.2.1 Pile ups

At high counting rates there is a possibility of two X-rays arriving at the detector almost simultaneously. When this occurs the X-rays are recorded as a single event with energy between that of the earlier event and the sum of the two energies, a problem leading to pile ups [Wat87]. Avoiding this spectrum distortion is a hassle but can be overcome by application of on-demand beam deflector. The beam deflection system momentarily holds the beam off the sample whilst processing of the previous event is on [Pro95].

2.8 Rutherford Backscattering

This is the most applied technique in ion beam analysis of non-microbeam work. RBS arrangement normally is when a beam of few MeV energy is projected on the target and for the energy of resultant particle to be measured by an annular-SBD placed at almost 180^0 at a backward angle. For a classical RBS elastic collision, a projectile does not have enough energy to penetrate the Coulomb barrier surrounding the nucleus.

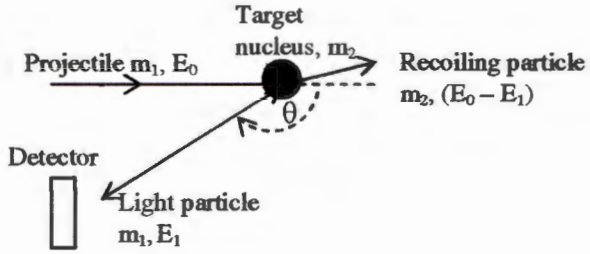

Fig 2.8 A schematic view of RBS analysis
[Wat87]

The scattering process is governed by the classical laws, with both energy (E) of the backscattered particle at angle θ and cross section ($d\sigma/d\Omega$) for the scattering to occur per unit solid angle defined by Rutherford scattering equations (Wat87 and Joh95);

$$E = \varepsilon_0 \frac{m_1}{(m_1 + m_2)^2}\left[\cos\theta + \left(\frac{m_2^2}{m_1^2} - \sin^2\theta\right)^{\frac{1}{2}}\right]^2 \quad \text{..... Eq 2.23}$$

$$\frac{d\sigma}{d\Omega} = 1.296\left(\frac{zZ}{E_0}\right)^2\left[\sin^{-4}\left(\frac{\theta}{2}\right) - 2\left(\frac{m_1}{m_2}\right) + \ldots.\right] mb.sr^{-1} \quad \text{..... Eq 2.24}$$

where

- m_1 and m_2 are the masses of projectile and target nuclei respectively

- E_0 is the energy of the projectile ion scattered at a given sample depth
- z and Z are the charges of the incident ion and scattering nucleus

Equation 2.24 is perfect for "normal RBS" (i.e 2MeV ^{4}He projectile) on elements with Z >11 but protons or deuterons often give non-Rutherford behavior [Wat87]. This explains the scarcity of such deviations' cross sections though there are some low-energy non-Rutherford cross sections. Due to the measuring of the resultant energy at a well-defined angle and known cross section, the technique gives advantages of correct scattering nuclei mass hence correct prediction of the sample stoichiometry. The other positive factor is the correct depth profiling as it (RBS) has a well-defined energy loss from electron collisions mainly [Joh95]. The RBS spectra are more difficult to interpret than PIXE spectra because dependence upon the mass of the scattering nucleus of the backscattered energy is nonlinear, with the kinematics of the scattering process making the masses of the heavier elements difficult to resolve (Joh95). The other complications could be that some resultant energy might be for something unexpected like a light element on the surface or a heavy element buried within the sample, therefore prior knowledge of the sample composition is vital. The analysis of the RBS spectra is being is facilitated by the simulation computer program called RUMP [Doo86].

2.8.1 Kinematic factor

When a projectile, of mass M_1, of zero acceleration collides elastically with a stationary target of mass M_2 the energy of mass M_1 will be transferred the target. In backscattering analysis, using principles of conservation of energy and momentum energy transfers can be quantified [Chu78]. The velocity and momentum of projectile M_1 are v_0 and E_0 (E_0 =1/2

M_1v^2) and M_2 is at rest. After collision velocities v_1 and v_2 and energies $E_1$and E_2 of ion and target atoms are determine by scattering angle θ and recoil angle [Fel86]. From figure 2.4, the conservation of energy and of momentum parallel and perpendicular to projectile angle we yield equations

$$\frac{1}{2}M_1v_0^2 = \frac{1}{2}M_1v_1^2 + \frac{1}{2}M_2v_2^2, \quad \text{.....Eq 2.1}$$

$$M_1v_0 = M_1v_1\cos\theta + M_2v_2\cos\phi, \quad \text{.....Eq 2.2}$$

$$0 = M_1v_1\sin\theta - M_2v_2\sin\phi. \quad \text{.....Eq 2.3}$$

After eliminating both ϕ and v_2, the ratio of particle velocities becomes

$$\frac{v_f}{v_0} = \left[\pm\left(M_2^2 - M_1^2\sin^2\theta\right)^{\frac{1}{2}} + M_1\cos\theta\right]/\left[M_2 + M_1\right] \quad \text{.....Eq 2.4}$$

$M_1 < M_2$, for which the plus sign holds, have projectile energies ratio of

$$\frac{E_1}{E_0} = \left[\frac{\left(M_2^2 - M_1^2\sin^2\theta\right)^{\frac{1}{2}} + M_1\cos\theta}{M_2 + M_1}\right]^2 \quad \text{.....Eq 2.5}$$

The ratio of the projectile energy after elastic collision to that before the collision, E_1/E_0, is called the kinematic factor K and its dependant on the projectile ratio to the target weight and on the scattering angle θ.

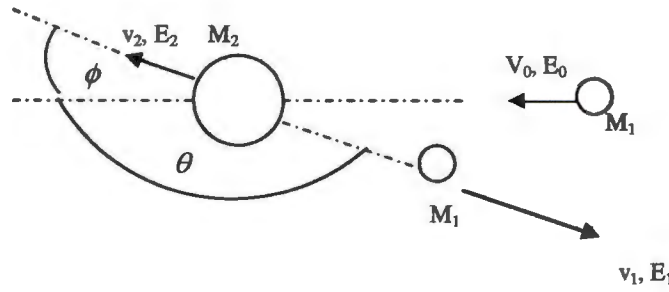

Fig 2.9 Diagrammatic representation of an elastic collision between incident ion of mass M_1 velocity v_0, energy E_0 and a target mass M_2 [Chu78]

2.9 Secondary Ion Mass Spectrometry

This technique is excellent for surface profiling. The process starts when a primary ion (projectile) of energy range 0.5 to 25keV interacts with a sample placed in a vacuum chamber at 10^{-9}Torr or below and secondary ions (products) are detected some distance away from impact site [Kri99]. Around impact site, surface depth ~3nm, bonds break and atoms random movement and displacement happens, a process called collision cascade. The collision leads to energy deposition, which is then returned to the surface as ejection of secondary ions transpires in a process called sputtering. Most ejected particles are neutrally charged but a lesser percentage is composed of singly charged and very large clusters of atoms with the singly charged dominating. If sputtered ions are clusters, then more internal energy will be needed to avoid disintegration if the distance between the source the detector is enlarged. The energy distribution differs according to the resultant secondary ions with the clusters peaking at slightly lower energy than singly charged. The clusters obviously being the heavier ions are detected from the upper layers whereas the more energetic light ions will surface from deeper layers.

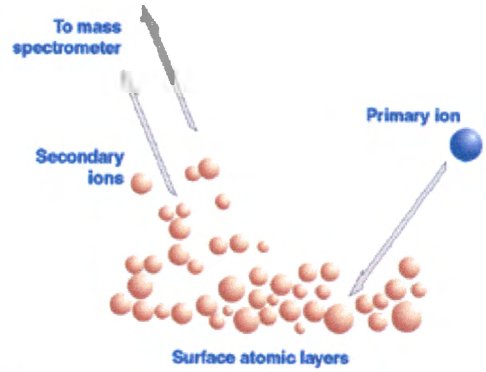

Fig 2.10 Schematic diagram of a SIMS process
[www5]

SIMS has relatively high lateral resolution because the sputtering primary ion beam is in micrometer range in diameter hence very small sputter area. It can be applied to all periodic table elements, and allow for measurement of many elements in the ppb-range. The technique is inherently non-quantitative, there is no simple relationship between given mass concentration and peak intensity. But for elemental species in a fixed matrix with low concentration range, the intensity ratio of elemental peak to that of matrix-related peak will follow a linear relationship with concentration. This allows for composition determination if a suitable standard calibration material is available. SIMS is a versatile technique, giving 3D information about the surface and near surface region of the material analyzed. It can be used for surface analysis (static SIMS), highly sensitive bulk (dynamic SIMS), depth profiling and analysis of lateral heterogeneity.

2.9.1 (a) Static SIMS

The aim is to minimize damage to the sample surface during data acquisition through the use of a very low primary ion current density. Less than 1% of the original sample surface is consumed during the course of the analysis. Material sputtered here is mainly in the form

of molecular fragments that reflect the surface chemistry of the sample. Thus it's possible to identify surface contaminants by their molecular fragments patterns.

2.9.1 (b) Dynamic SIMS

This is the second variant of SIMS where a primary ion current density is set as high as possible in order to maximize secondary ion yields. The surface is continuously eroded during analysis thereby changing the sample composition. It's an excellent depth profiler because by monitoring signals from elements as a function of time, depth profiles for those elements are obtained. Normally the projectiles are oxygen or cesium as these maximize the secondary ion yields of electropositive and electronegative species respectively.

2.9.1 (c) Depth profiling

This is the most sophisticated variant of dynamic SIMS. Shallow depth profiling is straightforward because the same ion gun is used for both erosion and analysis. It is considered as a dynamic SIMS variant as to do it you need to corrode the sample surface. Though one cannot fault it as much SIMS has also got its drawbacks, apart from being a surface analytical technique, its quantification is difficult except for the specific case of trace concentrations with calibration standards.

2.10 Scanning Electron Microscopy

Chemical analysis (microanalysis) in the scanning electron microscope (SEM) is performed by measuring the energy or wavelength and intensity distribution of X-ray signal generated by a focused electron beam on the specimen. With the attachment of the energy dispersive spectrometer (EDS) or wavelength dispersive spectrometers (WDS), the precise elemental composition of materials can be obtained with high spatial resolution. When we work with bulk specimens in the SEM very precise accurate chemical analyses (relative error 1-2%)

can be obtained from larger areas of the solid (0.5-3 micrometer diameter) using an EDS or WDS [www9]. In SEM technique the area to be examined or the microvolume to be analyzed is irradiated with a finely focused electron beam, which may be swept in a raster across the surface of the specimen to form images or may be static to obtain an analysis at one position. Types of resultant signals produced by interaction of the electron beam and the sample include secondary electrons, backscattered electrons, characteristic X-rays, and other photons of various energies [Gol03].

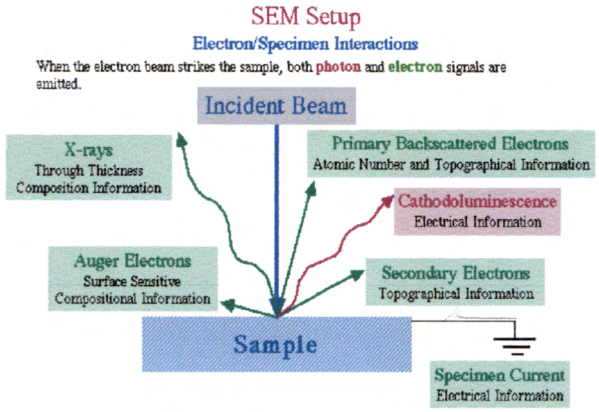

Fig 2.11 Scanning Electron Microscope Setup
[www6]

These products are obtained from specific emissions hence can be used to examine sample characteristics such as surface topography, crystallography, composition, etc. Backscattered and secondary electrons are of greatest interest in imaging because these vary primarily as a result of differences in surface topography. The three-dimensional appearance of the images is due to the large depth of the scanning electron microscope as well as to the shadow relief effect of the secondary and backscattered electron contrast. The analysis of the characteristic x-rays emitted from samples can yield both qualitative identification and quantitative elemental information from regions of a specimen nominally 1μm in diameter and 1μm in depth under normal operating conditions.

2.10.1 (a) SEM operations

A beam of electrons is produced at the top of the microscope by heating of a metallic filament. The beam then follows a vertical path through a column of a microscope and along the way it passes the electromagnetic lenses that focus it onto the sample. Once it hits the sample the already mentioned products will be detected. After interaction, detected electrons are converted into a signal that is then sent to a viewing screen whereby an image will be produced.

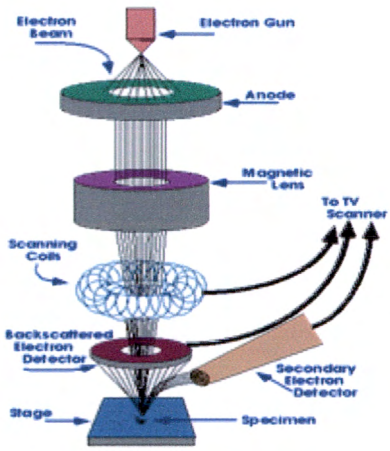

Fig 2.12 The Schematic Illustration of SEM Process
[www6]

All this is done in vacuum where air is sucked out to avoid beam instability caused by interaction of it (beam) and air molecules before bombarding a sample. Other problems maybe the burning of the electron source, ionizing of the beam molecules, defocusing of the beam.

2.10.1 (b) Sample preparation

Only conductive samples will be analyzed, but those that are not conductive will be put through a process to make them suitable. The process involves using sputter coating where a carbon layer will be placed on top of the sample. A neutral argon gas is passed through an

electric field and gets ionized. The ionized gas will then focus on the carbon layer thereby making the layer hence sample conductive.

Table 2.2 Nuclear microprobe analyses compared with other techniques. [Wat87]

Method	Detectable elements	Lateral resolution(μm)	Depth resolution(μm)	Depth range(μm)	Bulk limit(wppm)
NMP					
Particle-induced X-ray emission	Z > 11	~1	~5	~5	>0.1
Nuclear reaction analysis	All low Z	>1	0.005	1	>0.01
Rutherford back-scattering	Z >1	>1	>0.01	1	>0.1
Elastic recoil detection analysis	Z < 15	>1	0.005	1	>500
Other techniques					
Secondary ion-mass spectroscopy	All	0.05	0.005	2*	0.001-10
Auger electron spectroscopy	Z > 2	0.1	0.001	2*	1000
X-ray fluorescence	Z > 11	1000	5	5	1
X-ray photoelectron spectroscopy	Z > 2	1000	0.001-0.003	2*	1000
Ion scattering spectroscopy	Z > 2	100	0.003-0.001	2*	1000
Electron microprobe analysis	Z > 3	0.5-1	0.5	2*	100
Laser microprobe mass analysis	All	0.5	0.1	0.1	0.07-20
Synchrotron X-ray fluorescence	Z > 11	30	~5	~5	0.1
Glow discharge optical spectroscopy	Z > 5	1000	0.0003	2*	1000

* Successive analyses as new surface is exposed by erosion.

2.11 Historical Background Review

Boron concentration and depth profiling has been attempted before with a lot of success though there were problems encountered. This has spiraled from progress in geological

importance to biological, medical and even metallurgical [Jia02]. The cross-sections for the reaction, $^{11}B(p,\alpha_1)^{8}Be$, proved to be not realible as the available data showed errors of up to 30% and inconsistency of about 50% [Jia02]. Some of the pioneering work on the use of the nuclear reactions was done by N. Moncoffre [Mon92] but the cross-section data were initially enhanced by M. Chiari [Chi01] before L. Jiarui used a self-supporting ^{11}B absorber to measure them correctly. Chiari's work showed good correlation with previous work of Segel [Chi01], Mayer [Chi01] and others with uncertainty range of ±6% to ±8% recorded. As the availability of cross-sections increased, the use of ^{11}B also increased because boron could then be detected at lower concentrations with better accuracy. The use of the $^{11}B(p, \alpha_1)^{8}Be$ reaction showed to have interference from other nuclear reactions but has a broad resonance at E_p of 660 keV. The same reaction can also be used at E_p of 163 keV to depth profile boron due to the narrow resonance displayed [Mon90]. The broad resonance emanates from the resultant three alpha particles as reaction products [Mon92]. The reaction though is a powerful tool in detection of light elements due to the presence of a high cross-section (300 mb). This was put to test with excellent results by R. Lappalainen as boron concentration of 1 wt ppm was measured in biological samples [Lap85]. The results, lager cross-sections, became also important to the medical professionals as now cancer treatment could now have an alternative from boron neutron capture therapy (BNCT) which requires extra shielding meaning more expenditure. The nuclear reaction, $^{11}B(p, \alpha_1)^{8}Be$, was used to profile boron concentrations content by Sjöland and Wegdén [Sjö95] and [Weg04]. Using this reaction was a milestone achievement in geological studies as boron is a component of the earth crust. Results obtained using the reaction indicates that nuclear reaction analyses of silicates are virtually matrix-insensitive [Sko03].

Boron concentrations in geological samples were earlier measured individually by Kristiansson and Trompetter in 1999 followed by Hålenius in 2000. The PIN photodiodes have been tried before with good results acquired as detection limits of 5 ppm were observed [Szi04]. From the above mentioned reaction unexpected exit channels are possible depending on the conditions. This is because due to several broad resonances, the compound state of ^{12}C at any E_p is thought to be superposition of states hence the difficulty in clear-cut interpretation on the reaction [Dea57]

The exit channels observed are: $^{11}B + p \rightarrow {}^{12}C^* \rightarrow \alpha_0 + {}^{8}Be \rightarrow \alpha_0 + \alpha_{01} + \alpha_{02}$

: $^{11}B + p \rightarrow {}^{12}C^* \rightarrow \alpha_1 + {}^{8}Be^* \rightarrow \alpha_1 + \alpha_{11} + \alpha_{12}$

: $^{11}B + p \rightarrow {}^{12}C^* \rightarrow \alpha_2 + \alpha_3 + \alpha_4$

: $^{11}B + p \rightarrow {}^{12}C^* \rightarrow {}^{12}C + \gamma$ [May98]

Apart from the exit channels shown, there are other reactions which can be produced as shown by the following description (Figure 2.13).

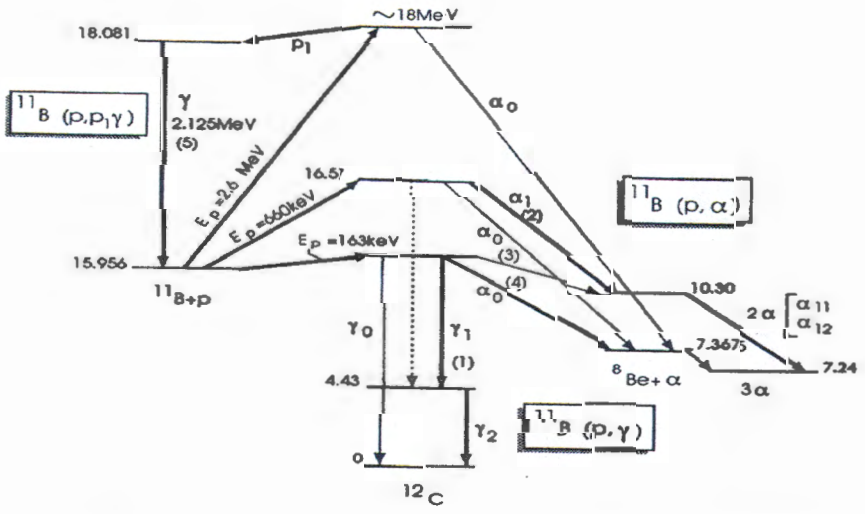

Fig2.13 Possible nuclear reactions with protons on ^{11}B. Thicker lines emphasize the origins of the nuclear reactions that can be used for analytical applications [Mon92]

Chapter 3

3.1 Experimental techniques and equipment

3.1.1 Standards

3.1.1.1 Sample preparation

Preparation of glass standards was done at Stellenbosch University. The glasses had 5 different boron weight percentages though the base material was of the same composition. The base material were composed of SiO_2 (78%), K_2O (10%) and Al_2O_3 (12%). Thereafter B_2O_3 of 10%, 5%, 2%, 0.5%, 0.1% was added to 5 equal parts of the base material respectively.

Sample thickness

The sample-holder (resin) is circular in shape, 4mm thickness and 24mm in diameter hence the energy loss has an effect on the final ejectiles detected. There is also the effect of non-homogeneity of the glasses which leads to non-uniform counts collection. The glasses are placed on the surface and are relatively very small.

Coating

The resin was then prepared for analysis by carbon coating in order to avoid charging problems. This was done using the Edwards Carbon Coater where the coating thickness can be assessed by the change of color to blue. After then a carbon connector is attached to transfer charge from the coated side to the other side of the resin. The only observed problem was the presence of Hg, Tl and Co introduced by the carbon coating.

3.1.1.2 NIST standards

The Standard Reference Materials (SRMs) No.612 and 614 were used purchased from the National Institute of Standards and Technology. They were produced and certified to

facilitate the development of chemical methods of analysis for trace elements. They are used for calibrating instruments and evaluating analytical techniques used to determine trace elements in inorganic matrices. Their nominal glass composition for all pairs is 72% SiO_2, 12% CaO, 14% Na_2O and 2% Al_2O_3 and they are 3mm thick. The materials were prepared in rod form and sliced into wafers. The wafers are oval-shaped in cross-section with nominal diameter 12-14 mm. As wafering includes cutting, some resultant debris are wiped with alcohol followed by surface cleaning with diluted HNO_3 (1:10). Since wafer cutting is done by copper-bonded diamond wheel, HNO_3 is again used to remove remaining copper contamination. In all pairs of SRMs boron, as all elements present, appears in wt%, ppm but boron is reported as informative values only. [www7 and Ree92]

3.2.1 LEO EDS-SEM procedure

Imaging and analysis of the phase compositions was done using a Leo® 1430VP Scanning Electron Microscope at the Stellenbosch University. Prior to imaging or analysis the samples were sputter-coated with carbon. Samples were identified with backscattered electron (BSE) and secondary electron images whereas phase compositions were quantified by Energy-Dispersive (EDS) X-ray analysis using an Oxford Instruments® detector with 133eV resolution and Oxford INCA software. Beam conditions during the quantitative analyses were 20kV electron energy and current of approximately 1.5nA, with a working distance of 13mm and a specimen beam current of -3.9nA. Despite the relatively low energy, X-ray counts in the set-up used were typically ~ 5000 counts/seconds. The counting time was 50 seconds live-time. Natural mineral standards were used for standardization and verification of the analyses. Pure Co, Ti and

Fe in ilmenite were used periodically to correct for detector drift. Beam conditions during semi-quantitative analyses were as described above without controlling the specimen beam current and the results were normalized to either 100wt% or by charge.

3.2.2 LEO SEM Variable Pressure Procedure

Variable Pressure operation is a SEM mode where the vacuum pressure in the chamber is higher than the vacuum in the column and gun. A fixed aperture is inserted between the chamber and the column and a different vacuum pump rate is applied for the chamber and the column. Small numbers of gas particles in the chamber are ionized by the electrons expelled from the sample and are then detected by the glass variable pressure detector. The beam conditions were an accelerating voltage of 25kVand a spotsize of 350nm, corresponding to approximately 1.5nA. The working distance that gives the best results is 7mm and the vacuum pressure in the chamber is set to 50 Pa to start off with. Variable pressure operation is appropriate for samples that are damp, kept in alcohol or soft samples that will loose shape during high vacuum conditions.

3.3.1 Nuclear microprobe

The microprobe is installed on a 6 MV single-ended Van de Graaf accelerator and uses a standard magnetic quadrupole triplet (OM 150) manufactured by Oxford Microbeams for beam focusing. For proton currents of 100 pA resolutions of the order of 1μm beam spot can be obtained and also currents of the order 10nA are possible for beam spots not exceeding 10 μm. Relatively large scan sizes (e.g. up to 2.5 × 2.5 mm for 3 MeV protons) are possible. The target chamber is the standard Oxford NMP chamber, modified to allow fast changes of specimen position using stepper motors. A built-in wheel accommodates up to 10 absorbers, usually interposed between the detector and the specimen to reduce

the intensity of the X-rays from lighter elements, present as major components. Charge collection is carried out using a sensitive electrometer that measures current simultaneously from a Faraday cup behind the sample and from the insulated sample holder [Pro95]. Diagram description of the nuclear microprobe beam line is displayed in figure 3.1.

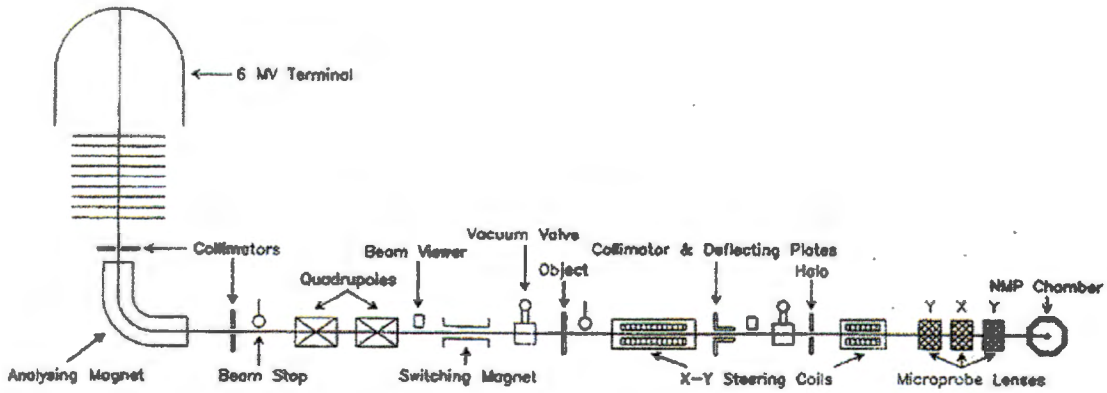

Fig 3.1 A schematic representation of the Van de Graaff accelerator and NMP layout at iThemba Labs. [Pro95]

The Van de Graaff accelerator at iThemba Labs accelerates ions vertically downwards and energy selection is done by a 90^0 analyzing magnet. Ions then travel through a horizontal flight path of about 15m to the target [Pro95]. This long distance is beneficial for ultimate beam spot sizes obtainable but it also makes the nuclear microprobe susceptible to beam instabilities, which, in a vertical accelerator configuration leads to vertical movement of the beam [Pro95]. After passing through the analyzing magnet, collimators, quadrupole doublet, and switching magnet respectively it goes through the variable slits before the object slits. The aim is to minimize the amount of the current passing to the object slits as the latter can handle maximum of 100nA whereas the accelerator can produce currents in excess of 1μA. The variable slits act as a regulator because they can be closed when the current is too high or be opened if it is not critical in

order to allow more ions to impinge on the target. The target chamber is pumped down by the turbomolecular pump supported by the roughing pump with pumping time, to pressure of 5 $\times 10^{-5}$ torr, of less than 5 minutes [Pro95]. The chamber has the following features:

- X-ray detector situated 22mm away from the target at 135^0 to the incoming beam
- An annular Si surface barrier detector situated at an angle close to 180^0
- Channeltron electron detector for secondary electron imaging
- Electron suppression ring in front of the target and the optical microscope at 45^0 with respect to the normal to the sample surface [Pro95].

The lighting in the chamber is provided by the reflected and transmitted lights whereas sample loading is done with the aid of a removable lid for easy access of the ladder carrying the samples. The stepper motors control the samples in the X, Y and Z axes and allow easy and fast access of permanent set of standards which are used for calibrating purposes. Signals from the detectors are fed to the normal electronic units for amplification and digitization.

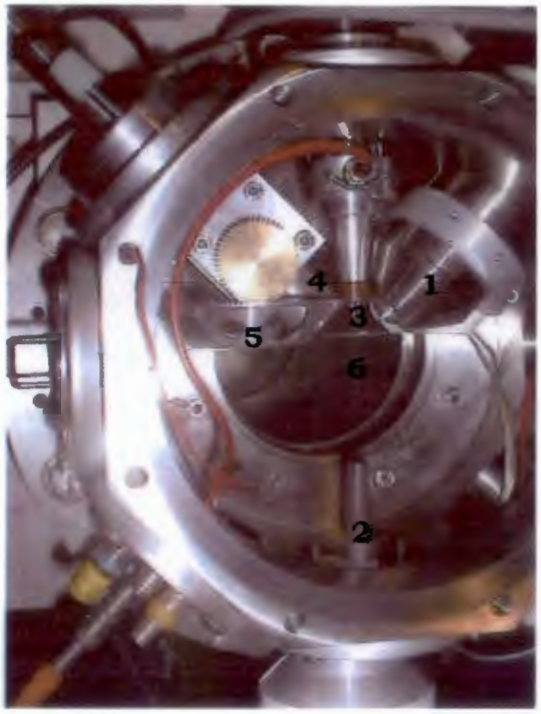

Fig 3.2. The inside of the MRG NMP Chamber: 1. Optical microscope, 2. Faraday cup, 3. Electron suppressor, 4. PIXE detector, 5.Filter wheel, 6. Target position

3.3.1.1(a) On-demand beam deflection system

A vertically mounted machine's main problem is the beam ripple which leads beam instabilities hence problems related to electronic processing of signals at relatively low count rates. The addition of beam deflection system is meant to regulate the deadtime to low percentages in ion beam analysis and higher count rates. The mechanism of the beam deflection system is to allow the beam to pass between two zero potential plates onto the target. After processing of an event in the X-ray detector, plates quickly charge to equal voltages of opposite polarity. This deflects the beam from the target thus allows spectroscopy amplifier time to process the same event, with probability of another signal in this time only arising from the finite loop time, determined by the time taken for fast processing of the event, plates charging and flight time of the ions already through the plates. The beam on-demand design minimized the distance between the plates and target

to 2m. The plates are protected by the collimator which also acts as a beam divergence limiter [Pro95].

3.3.1.1 (b) Beam instabilities

Beam instabilities related to vertical movement have an effect on the accelerator performance. Any energy variation in the downward acceleration phase is transmitted as movement in the Y-direction [Pro95].This movement leads either to movement of the beam on the sample or pulsation of the beam on the target which is the reason the beam on-demand deflection system was installed.

3.3.1.1 (c) Data acquisition and analysis

The XSYS data acquisition system allows for use of complex arrays of data, event-by-event storing capability, use of multi-parameter systems and multiple windows. Event handling is managed by EVAL language code supported by VAX computer network. The XSYS and VAX are linked by the CAMAC crate.

Data analysis programs for NMP are GeoPIXE for analysis of X-ray spectra, RBS spectra are analyzed using RUMP and NRA data are analyzed using either the LORIG or SENRAS, but for this study GeoPIXE will be used [Pro95].

Nuclear microprobe is a versatile facility which can be used by geologists, biologists, physists, etc. Its chamber can be re-aligned to accommodate even what was originally not planned for; e.g introduction of different detectors for a particular experiment. The introduction of such apparatus obviously needs measurements and understanding of the instrument before installation. For this study Si PIN Photodiodes were installed. Though this change affects the geometry, important precautions were taken to make sure of the

feasibility of using the annular-SBD, the PIXE detector and the microscope at the same time.

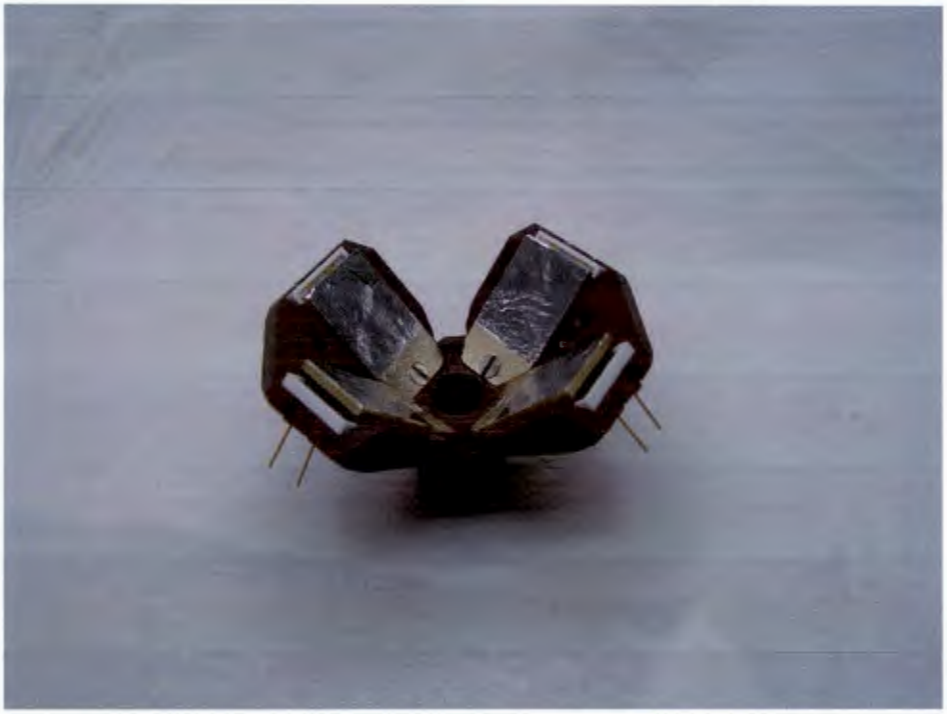

Fig.3.3 Si PIN photodiodes detector at MRG NMP Chamber, iThemba LABS

These commercial detectors, HAMAMATSU-S3590-02, were selected because of their advantages which includes the feasibility of optimizing the solid angle and are cheaper compared to the annular-Surface Barrier Detector. Their negative sides are necessity for protection against light and relatively poor resolution. The detectors are connected in parallel and mounted on an insulating backing with nominal active area of each diode being 10 ×10mm^2 [Szi04]. Due to their construction, windowless and separated, the filter for absorption of backscattered protons during the running of an experiment had to be added. Aluminium kitchen foil was used but before, a SRIM calculation was done to evaluate energy loss of projectile on a certain Al foil thickness.

Table 3.1 Al foil Stopping Range of Ions in Materials (SRIM) Calculations[1]

Aluminium SRIM Calculations			
Ion Energy (keV)	dE/dx(Electronic)	dE/dx(Nuclear)	Projected range(um)
650.00	2.2×10^{2}	1.81×10^{-1}	7.77
660.00	2.18×10^{2}	1.79×10^{-1}	7.93
670.00	2.16×10^{2}	1.76×10^{-1}	8.1
675.00	2.16×10^{2}	1.75×10^{-1}	8.19
680.00	2×10^{2}	1.74×10^{-1}	8.27
690.00	2.13×10^{2}	1.72×10^{-1}	8.44
700.00	2.12×10^{2}	1.70×10^{-1}	8.62

[1] ***Longitudinal and lateral straggling columns have been omitted.***

SRIM calculations were first done to assess the thickness of Al foil needed to stop backscattered protons. Al foil used for cooking was next used as an absorbing layer. The thickness of this foil was obtained by:

1. measurement using vernier caliper
2. weighing a square piece of foil
3. measurement using proton backscattering, using 3 MeV protons (energy of available alpha particles was too low for penetrating the foil).

The obtained values were 10.74μm, 9.259μm and 11.4μm respectively. They obtained by converting mg/cm^2 to micrometers except for method 1 of thickness. From the resultant comparison of projected range and thickness calculations, we can assume that indeed the Al foil can be used as an absorber.

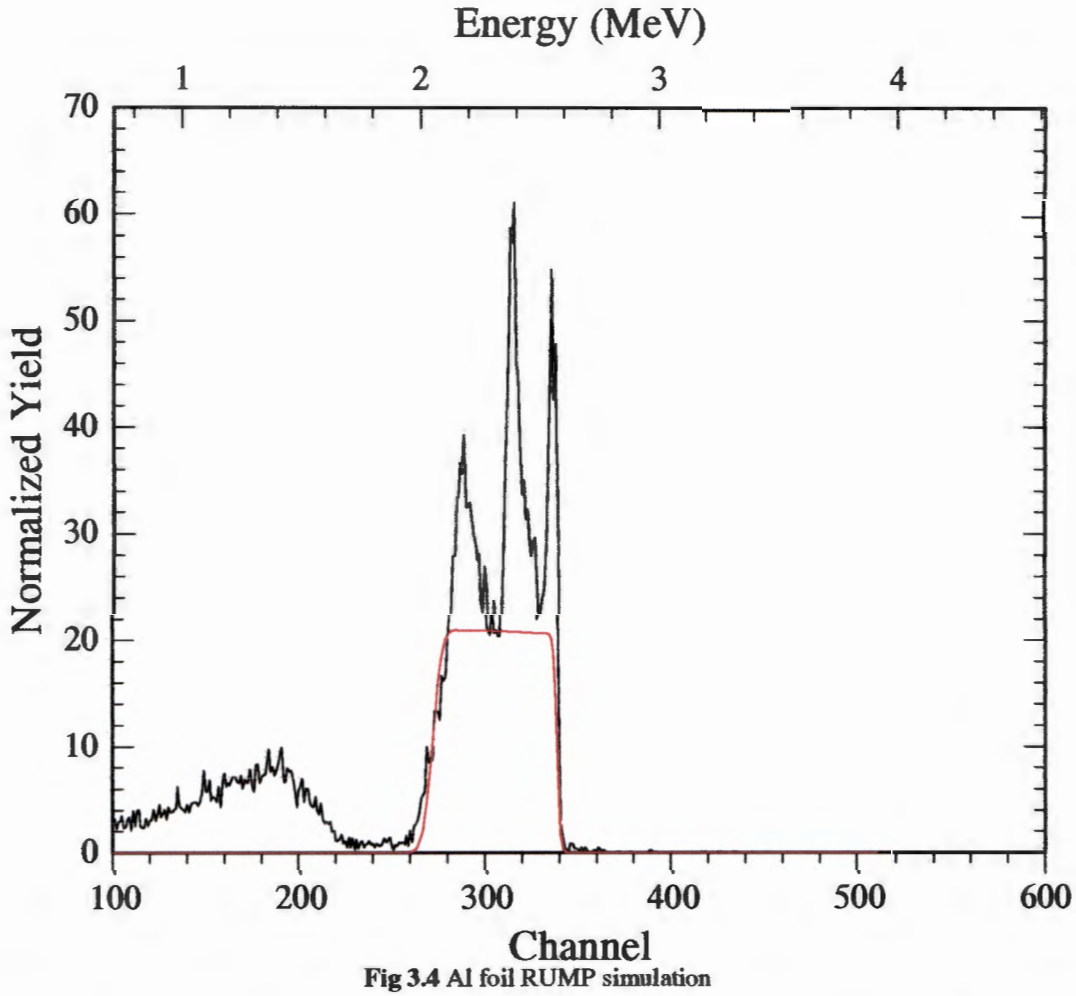

Fig 3.4 Al foil RUMP simulation

With the stopping range of protons being sorted, it was ideal to use again SRIM to find the range of alpha particles generated in the reaction $^{11}B(p, \alpha_1)\ ^{8}Be$. This is because they (α-particles) are expected to have a range of energies; α_1 has 3.63MeV at 172^0 whereas $2\alpha_2$ have energy range from 4.48MeV to 6.2 keV but all 3α's are detected simultaneously [Mon92]. The α_1 energy is subject to change depending on the angle of detection, it is 4.1MeV at 90^0 [Cha95]. That can be attributed to the angular correlation function between α_1 and $2\alpha_2$ which can be related to energy distribution of the continuum α-particle spectrum by observing process dynamics [Dea57]. Process dynamics steps: Initially motion of compound nucleus (3α's) in the direction of projectile ^{+}H with

velocity $\mathbf{v}_1$; then dissociation of 3α's with ^{8}Be* recoiling with velocity $\mathbf{v}_2$ in opposite direction to the α_1 particle; lastly break-up of ^{8}Be* nucleus, with final particles $2\alpha_2$ emitted with velocity $\mathbf{v}_3$ at an angle θ relative to the direction of $\mathbf{v}_2$.

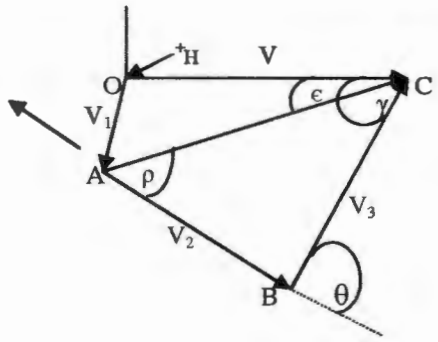

Fig.3.5 Velocity diagram for nuclear reaction ^{11}B(p,α) ^{8}Be* [Dea57]

From the information of recently mentioned literature, it is obviously clear that with our experiment preparation we expect to get almost similar α_1 energy values because of the geometry, see fig 3.6 below. The top and bottom pairs cover an angle of 72^0 each and sideways, two angles of 108^0 each.

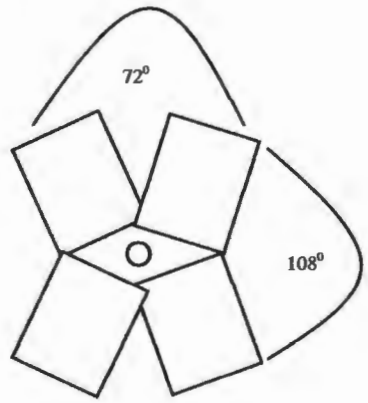

Fig.3.6 Angles covered by the Si PIN photodiodes at NMP, MRG

Table 3.2 below shows the stopping ranges from alphas of a decaying Thorium-228 source.

Table 3.2 Stopping Range of Ions in Materials (SRIM) Calculations for Al foil[1]

Aluminium SRIM Calculations			
Ion Energy (MeV)	dE/dx(Electronic)	dE/dx(Nuclear)	Projected range(mm)
5.3405	4.99	1.816×10^{-03}	61.38
5.4233	4.93	1.791×10^{-03}	63.05
5.6856	4.78	1.715×10^{-03}	68.45
6.0510	4.57	1.619×10^{-03}	76.26
6.2883	4.46	1.563×10^{-03}	81.51
6.7785	4.24	1.459×10^{-03}	92.79
8.7840	3.59	1.149×10^{-03}	144.43

[1] ***Longitudinal and lateral straggling columns have been omitted.***

Chapter 4

4.1 Results and discussion

Different samples were used as standards during the study. There were the resin-embedded glasses, Boron Nitride (BN), tourmaline and the National Institute of Standards and Technology (NIST) standards. This was done to have a bigger range of boron concentration. There was also measurement of a plate glass to counter the problem of oxygen interference.

4.1.1 SEM and EDS

Data obtained proved a major help in assessing the contents of our standards, that is, the weight percentages of our elements in prepared standards. This was done using Energy Dispersive Analysis (EDS) to complement Scanning Electron Microscopy (SEM). The anticipated boron weight percentages were 10, 5, 2, 0.5 and 0.1 for glasses 1, 2, 3, 4 and 5 respectively but after the EDS was done; obtained values proved that indeed there is a possibility that there were some errors done during preparation, see table 4.1. This proved vital since the calibration curve would have not corresponded to what was expected, hence wrong conclusions concerning concentrations in unknown samples. Therefore the calculated values taken as boron weight percentages were 9.52, 7.97, 4.7, 1.99 and 0.629 in that sequence for glasses 1, 2, 3, 4 and 5 respectively. Before SEM, the optical microscopy was used to locate all the glasses on the epoxy, see figure 4.1. The importance of using this technique (SEM/EDS) is because in optical microscopy though you can find the glasses; you don't get to know how smooth and homogenous the glass is. The importance of SEM can be undermined when it comes to the above-mentioned weight percentages because it is mostly excellent with major elements analyses

(>10wt%) see figure 4.2 below, but with the pictures obtained we can then focus the electron beam on homogenous phases of the glasses. This means though we are not analyzing the whole sample, at least we focusing on where we expect all of the elements to be.

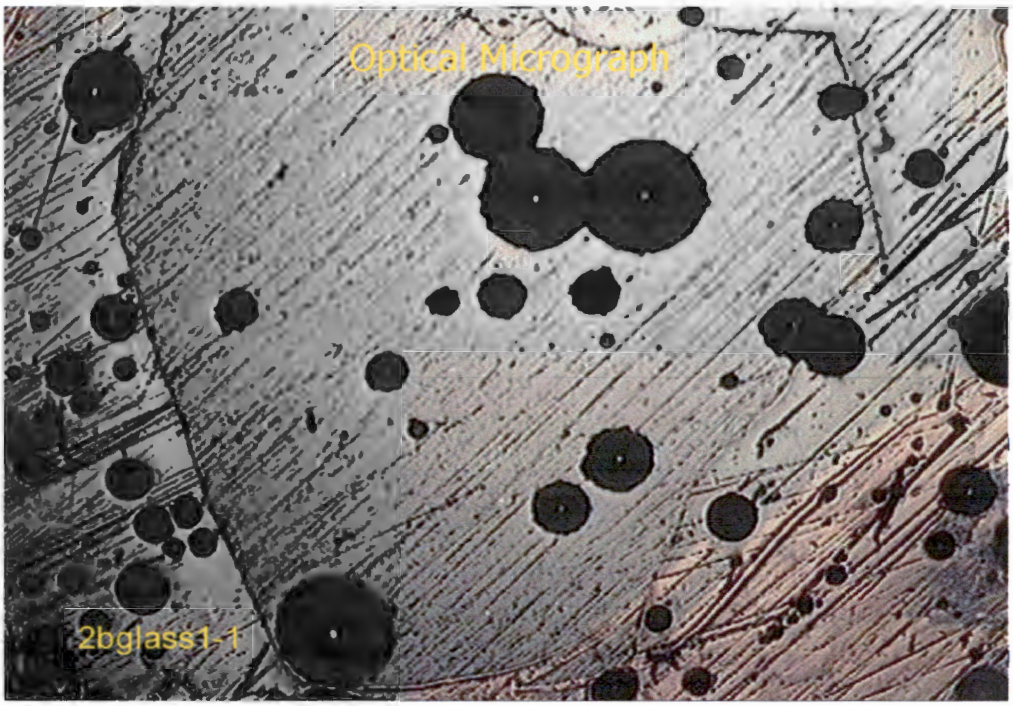

Fig.4.1 Optical micrograph of glass 1 (~10wt %)

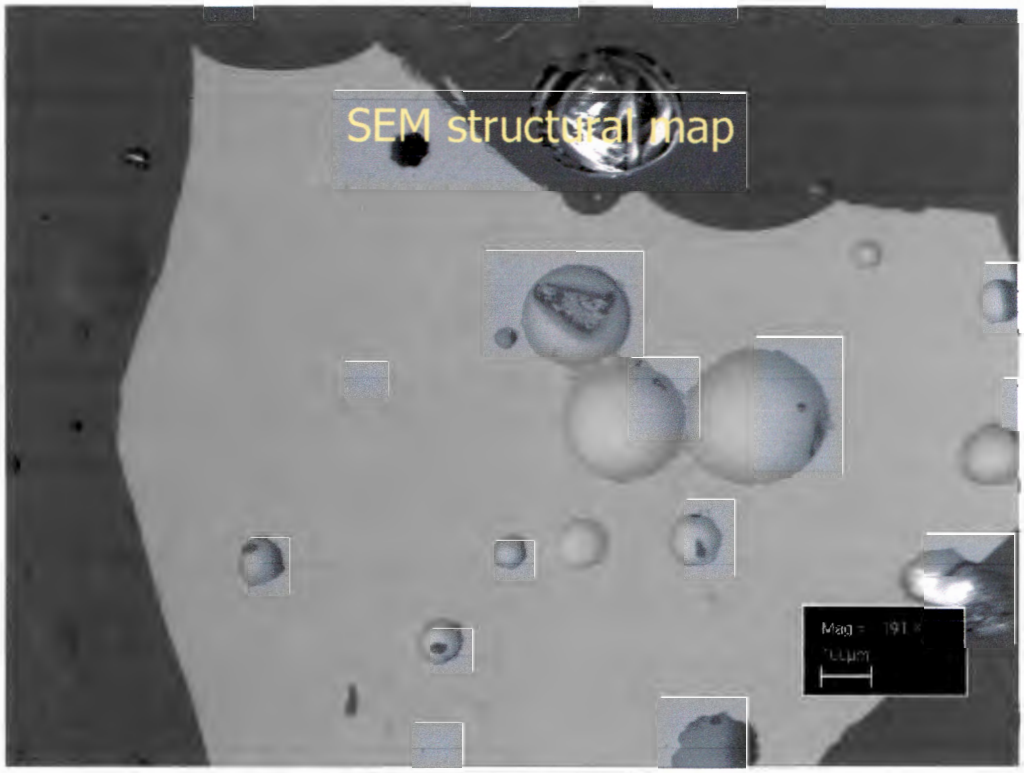

Fig.4.2 SEM structural map of glass 1 (~10wt %)

Analyses of low boron concentration with EMP were impossible because of high detection limits hence BN was measured first in order to have the optimal conditions for boron analysis. Then modify the conditions to suit standards with low boron concentrations. Optimal conditions included the adjusting pulse shaping parameters and longer shaping time which allowed for boron detection for the first time since commissioning of the Stellenbosch University facility.

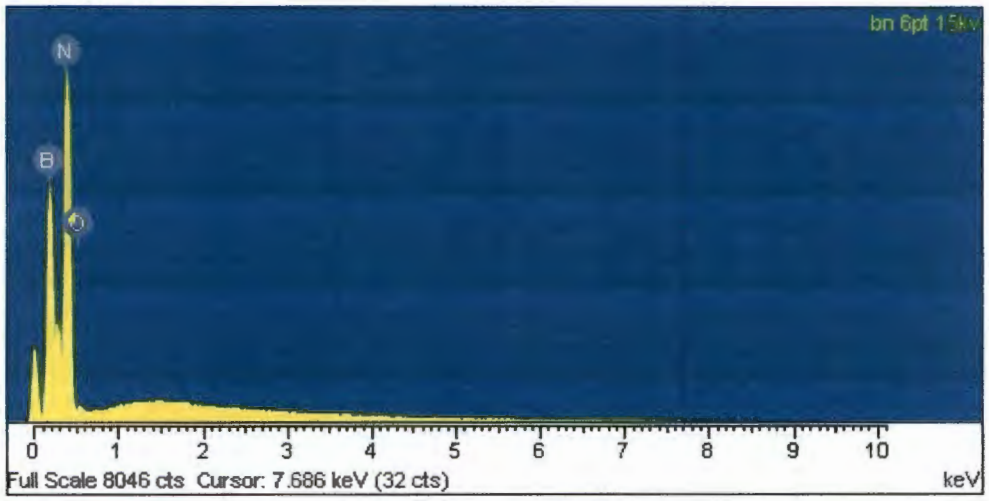

Fig.4.3 SEM spectra of BN

With the conditions set for boron peak, the next aim was to measure boron glasses and in boron glass of 9.52wt % concentration in particular where the spectrum below was seen. The clear peak of a BN gave a positive outlook, confirming that the facility can detect trace elements which contradicted what was initially perceived. The software showed some deficiency as 9.52wt % boron glass couldn't be detected though the conditions were optimally the same as there were for BN. Due to that, the software was fed with information of boron presence and that's when a boron hump appeared, figure 4.4. The subsequent measurements (for other glasses) no hump could be seen because according to the EDS only the first glass had boron elemental abundance weight percentage of 11.2 (table 4.2) which is larger than the benchmark for EMP (> 10wt %).

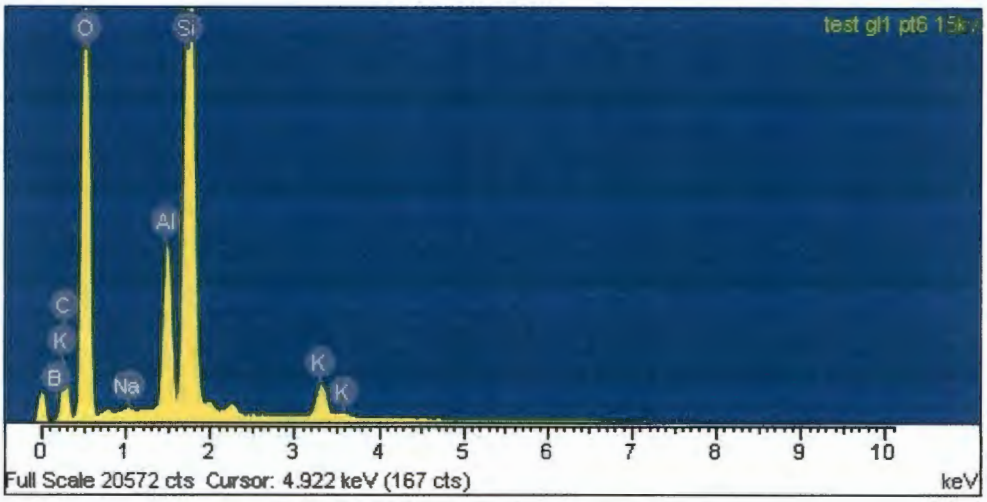

Fig.4.4 SEM spectra of glass 1(~10wt %)

Below, in Table 4.1, are the calculated chemical composition and the final values of boron weight percentages that are going to be used for plotting the calibration curve and their concentration will be compared to those obtained from EDS. The calibration curve is used to see the relationship or correlation between the trace boron levels (eg from samples) to the major levels (eg from tourmaline) obtained from the EMPA analyses. The EDS values (for heavier elements) can be applied to attain the structural formulae from average compositions [Kri99]. The stoichiometry can be used to obtain the structural formulae.

Table 4.1 Chemical composition and calculated B_2O_3 weight %

Glass 1	$Si_{0.03735}Al_{0.01214}K_{0.01009}B_{0.0058}O_{0.17999}$	9.52
Glass 2	$Si_{0.03735}Al_{0.01214}K_{0.01009}B_{0.0048}O_{0.17899}$	7.97
Glass 3	$Si_{0.03735}Al_{0.01214}K_{0.01009}B_{0.0028}O_{0.17699}$	4.7
Glass 4	$Si_{0.03735}Al_{0.01214}K_{0.01009}B_{0.0011}O_{0.17529}$	1.99
Glass 5	$Si_{0.03735}Al_{0.01214}K_{0.01009}B_{0.00035}O_{0.17454}$	0.629

4.1.1.1 Elemental abundances

The results obtained using EDS showed deviations from the calculated values and that culminated in a skewed calibration curves. The skewed lines are because of the non-correlation between the obtained B_2O_3 weight percentages and the corresponding normalized counts. The values were all appearing in an oxide form. The total values are the ones giving a convincing report on the errors made during weighing. It must be maintained though that the elemental abundances are not corresponding to the final calculated B_2O_3 values, and this is possibly due to the fact that not only boron oxide but all sample components were incorrectly weighed.

Table 4.2 Elemental abundances in weight percentages (EDS values) – Values measured to detect Boron, obviously not very accurate as the totals are wrong

Spectrum	B	Al	Si	K	O	Total
Glass -1	11.2	4.9	33.4	5.3	68.3	123.1
Glass -2	7.2	5.1	33.6	5.4	59.9	111.3
Glass -3	6.3	3.9	35.6	4.3	58.8	108.9
Glass -4	5.1	3.4	36.6	3.9	56.7	105.5
Glass -5	3.1	4.8	34.5	5.7	51.7	99.8

Table 4.2 cont.

Spectrum	B_2O_3	Al_2O_3	SiO_2	K_2O	Total
Glass -1	36.0	9.3	71.5	6.4	123.1
Glass -2	23.2	9.7	72.0	6.5	111.3
Glass -3	20.1	7.3	76.2	5.2	108.9
Glass -4	16.3	6.4	78.2	4.7	105.5
Glass -5	10.1	9.1	73.8	6.8	99.8

With the errors attained, data were normalized to see the amount of boron oxide introduced to the base material as compared to the values expected. The values in table 4.2 were normalized by charge but were not corrected to 100%. From table 4.5 with calculated and normalized boron values, the absent difference (total column) for the 4 glasses can be attributed to the Sodium (from possibly contamination) found when an average analysis of each of the glasses was done. From Table 4.3, the elemental

abundances are added to raw data (corrected/adjusted weighed values) so as to reach an oxide sum of 100% but as it is evident that the problem of difference between calculated and EDS' values still exist. This is because the data was not subjected to ZAF correction procedure.

Table 4.3 Elemental abundances from EDS in weight percentages (normalized data) - data normalized from table 4.2 above to give a total of 100 wt% - which you would expect if all the elements were measured correctly and accounted for.

Spectrum	B_2O_3	Al_2O_3	SiO_2	K_2O	Total
Glass -1	29.2	7.5	58.1	5.2	100.0
Glass -2	20.8	8.7	64.7	5.8	100.0
Glass -3	18.5	6.7	70.0	4.8	100.0
Glass -4	15.4	6.0	74.1	4.4	100.0
Glass -5	10.1	9.1	73.9	6.9	100.0

The base material values in all tables, bar table 4.4, will definitely be taken to be unreliable because it is expected that they should be the same for all glasses as the preparation for the base material was done once and the product divided into five equal parts. The table 4.4 base material values can be taken to be correct because they are constant for all glasses but the totals are skewed as they don't add-up to exactly 100%. This can be because during preparation of base material the assumption taken was that in 1 gram there will be a certain amount of each oxide compound but the truth is the totals for those oxide compounds were exceeding 1 gram. The assumption was obviously based on the calculations preceding the preparations. From table 4.3, the base material values are not consistent for all glasses. There are also huge B_2O_3 values for all the glasses. Even though a boron peak is expected for glass 1 in table 4.2, there is none but for the rest of the glasses it's no mystery because the boron percentage is less than 10wt %.

Table 4.4 Al, Si and K real values - Boron taken from table 4.3 plus Al, Si, K from table 4.3 replaced with what was calculated when glasses were prepared.

Spectrum	B_2O_3	Al_2O_3	SiO_2	K_2O	Total
Glass -1	29.2	9.6	77.5	6.8	123.1
Glass -2	20.8	9.6	77.5	6.8	114.7
Glass -3	18.5	9.6	77.5	6.8	112.4
Glass -4	15.4	9.6	77.5	6.8	109.3
Glass -5	10.1	9.6	77.5	6.8	104.0

Table 4.5 Recalculated and normalized Boron values from real Al, Si and K values - Normalized table 4.4

Spectrum	B_2O_3	Al_2O_3	SiO_2	K_2O	Total
Glass -1	23.7	7.8	62.8	5.5	99.7
Glass -2	17.9	8.3	66.7	5.8	98.7
Glass -3	16.5	8.5	69.0	6.1	100.0
Glass -4	14.0	8.7	70.5	6.2	99.5
Glass -5	9.7	9.2	74.4	6.5	99.8

The values from the recalculated (table 4.1) and normalized tables (table 4.4) shows a contradiction to calculation done for B_2O_3 (table 4.5) which means that either the calculations where wrong or the technique is not excellent in profiling sensitivity. From the standard preparation method, the observed errors in weighing are totally different to what is being shown by the EDS elemental abundances. This shows though the technique is good it's not the ultimate in EMP for elemental composition. The other technique such as WDS can be implemented for further clarification.

4.2 PIN Photodiodes Calibration

Due to the sensitivity of the PIN photodiodes detectors, it was imperative that before calibrating to find suitable and optimal operation conditions. As the XSYS system was used mostly for two measurement channels only in the nuclear microprobe RBS and PIXE, the other objective was find a channel that is suitable enough for reading counts from the PIN photodiodes. Two electronic measurements "channels" were tested and

calibrated using radioisotope sources, Am-241 and Th-228. The measurements "channels" used by XSYS data acquisition were:

1. Normally used for RBS and SBD

2. Normally used for PIGE; but for this study used NRA and PIN diodes.

There were a lot of adjustments on the default settings and the electronic equipments like lowering of energy threshold and Canberra 2020 amplifier respectively. . The use of an ORTEC Model 124 pre-amplifier proved good as the initial one, type EURISYS PSC 762-2F failed. During calibration there were noise problems observed on the NRA channel and this emanated from computer monitors, problems with earth loops in the nuclear microprobe electronics and light. This is because the PIN diodes are too sensitive. Though there was no default settings adjusted on RBS channel, the channel was also used during calibration because the idea was to compare between the two channels. Testing was initially done using a PIN diode with absorber were it was noticed that even the absorber (Al foil) had an effect on the resolution of the detector. From using the Thorium source (Th-228), which has 7 clear peaks ranging from 5.34054 to 8.78437 MeV, the diode with no Al foil showed better resolution. Calibration was also done on the a-SBD to see the difference between the two detectors. (See appendix for a-SBD resolutions)

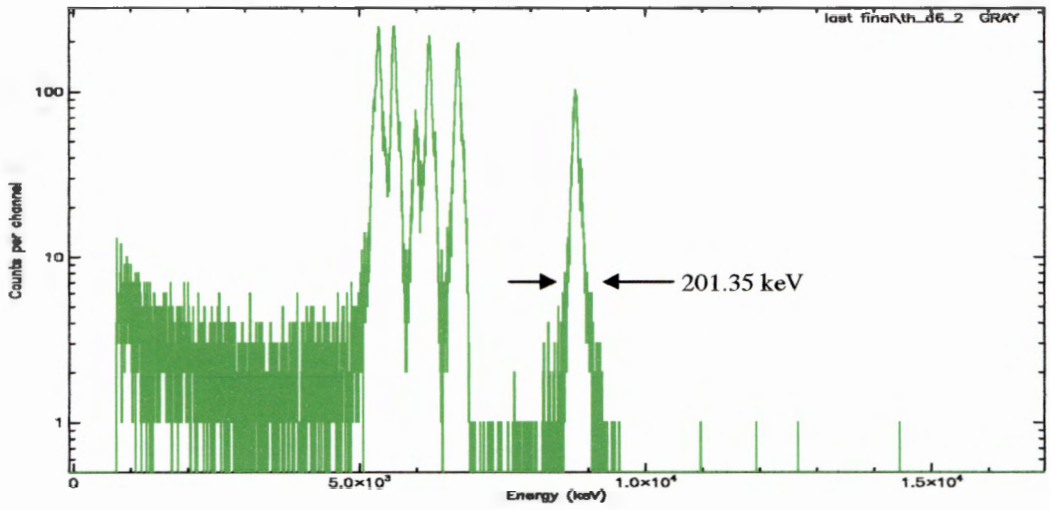

Fig.4.5 Thorium source spectra of PIN diode without an Al foil

From the above the next objective was to obtain a spectrum with absorber on but with as less noise as possible with the noise on the oscilloscope was at 200mV after earthing was implemented. After opting for an absorber a lot of noise was observed hence the subsequent spectrum. The Al foil does reduce the resolution; the effect of foil can be seen on figure 4.6 in comparison with figure 4.5.

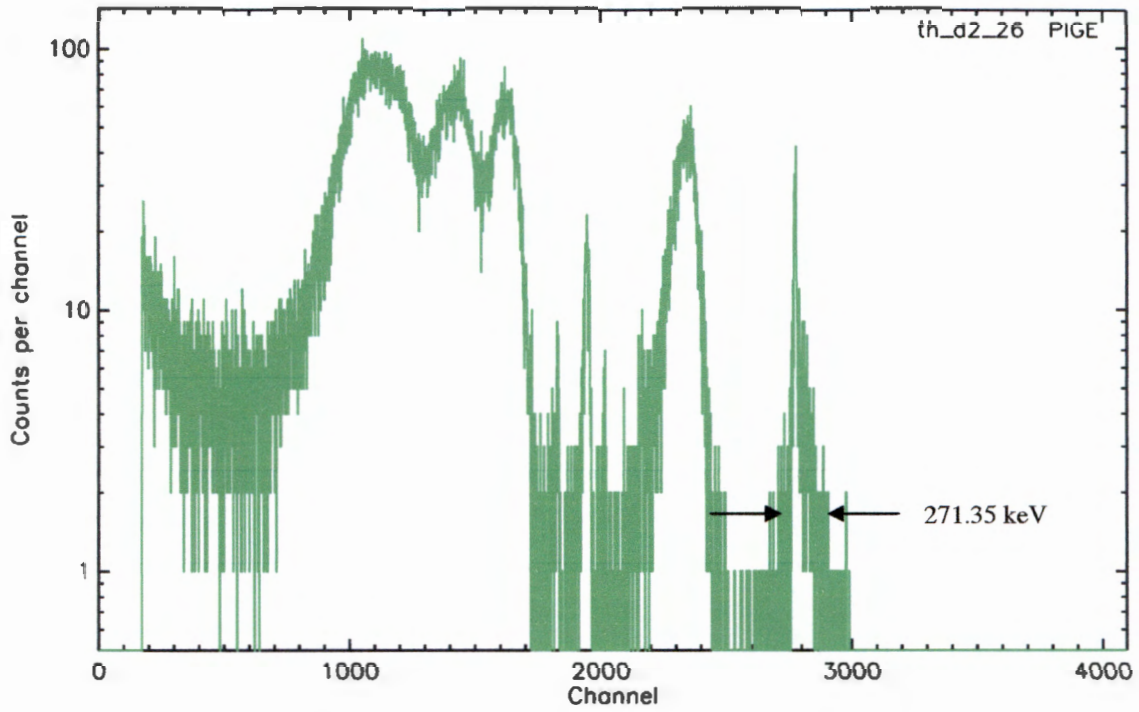

Fig.4.6 Thorium source spectra of PIN diode with Al foil

Though a lot of noise was observed, the peak close spectrum-end showed that not only is the noise from absorber but something else which was not proven. Then obviously the use of the whole array for testing might prove that because initially the testing was done with a single diode. The resultant spectrum (of the whole array), figure 4.6 proved that because similar resolutions were attained, see table 4.6. The other hassle was to include as much as possible of what was thought to be lost by virtue of the first peak starting at around 3000 keV.

Decreasing the low level discriminator did this but then there was noise problem when this is done a touch further than intended. The ideal energy level to start with will be around 3000 keV as below that we expect inference from Oxygen whereas at energy of

beyond 7.4 MeV there should be appearance of Lithium which should be observed in a tourmaline sample [Tro99], but obviously that will depend on the calibration of a particular microprobe facility. The use of Th-228 for calibration helped deduce the resolution of Si-PIN photodiodes as their peaks were clear and their resultant energy was of the required range. The poor resolution anticipated from the Si-PIN photodiodes was observed for both the Al-coated and the uncoated though it must be mentioned that for the latter a single diode was used. The single diode though had better resolution maybe because of the fact that the active area was small compared to the quad PIN photodiodes with Al foil.

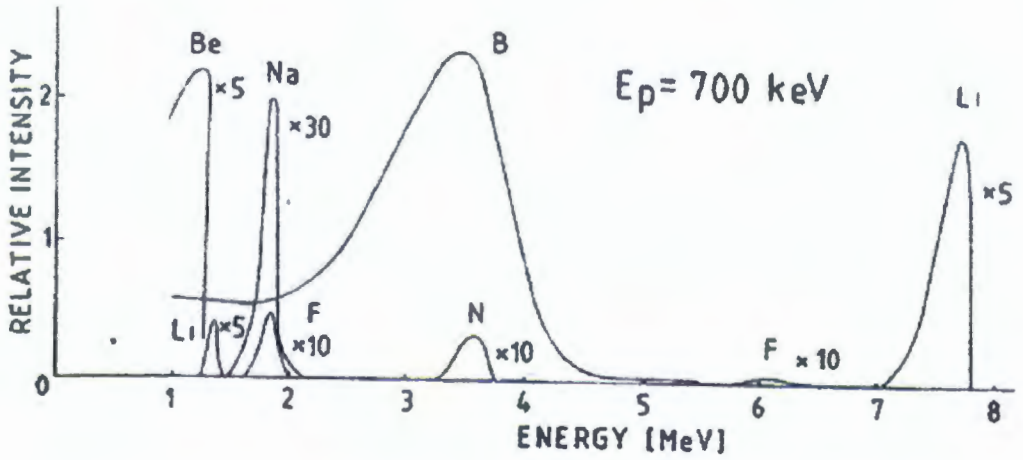

Fig.4.7 The figure showing the position of boron at Ep = 700 keV
Lap85

Table 4.6 Resolutions obtained for different PIN diode conditions

Single diode without Al foil	201.44 keV (see fig 4.5)
Single diode with Al foil	271.35 keV(see fig 4.6)
PIN diode array without Al foil	201.44 keV
PIN diode array with Al foil	271.35 keV

4.3 NRA results using annular-Surface Barrier Detector

The experiments were done at 6MV van de Graaff accelerator at Material Research Group, iThemba LABS. They were divided into two in order to have results using different detectors so as to compare results attained. For the initial experiment, an annular- Surface Barrier Detector was used. Beam conditions were that proton incident beam energy of 675 keV, beam current of approximately 200-pA to avoid pile-up and keep particle flux low on the detector, similar conditions to the conditions applied by Sziki [Szi04]. Due to the fact that normal applied energy is 3 MeV, the focusing magnets were adjusted for this lower energy to avoid deflection off axis caused by stray magnetic fields [Sjö97]. Using Labview computer software, scan sizes of $991 \times 1422 \mu m^2$ were attained. The accumulated charge ranged from 1 to > $9\mu C$ across all the sample glasses. The conditions of all hardware, i.e ADC, preamplifier, amplifier, etc were default with no adjustment because we were mainly concerned with the RBS spectra.

The second part of the experiments had almost similar conditions except that this time the PIN photodiodes had been installed. Other differences included installation of new ADC, preamplifier, amplifier, etc. Because of new addition of hardware, necessary adjustments were done for acquisition of events from the detector to the XSYS.

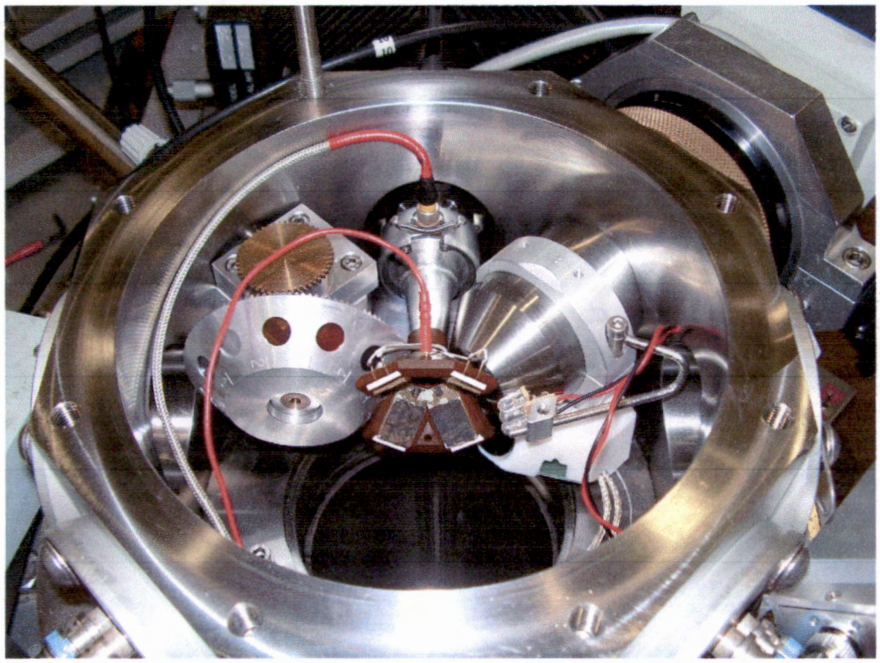

Fig.4.8 A Nuclear Microprobe Chamber with mounted Si PIN photodiodes detector at Material Research Group, iThemba LABS

From the testing results it was more sensible to analyze, with the nuclear microprobe, initially the standard with large stoichiometry boron concentration (9.52wt %). This is because it would be easy to get boron events. The NRA analysis was done in two steps: the energy window (between 3 and 5.5 MeV) was selected, and then every event in the region was used to define the area where Boron is located. Secondly, both the numbers of B and charge events in every pixel of the selected area are counted and their ratio (B-counts/charge) is calculated, figure 4.9. If data storage is done in time sequence mode, it is possible to discard those counts that are offline and normalize the boron yields [Sko03]. With the energy regions for different reactions selected, we expect the boron events to be in the energy region 3 to 5.5 MeV and the lower energy region to be for backscattered protons. Contributions from possible interfering reactions involving ^{15}N

and ^{18}O are considered negligible because their yield must be greater by three orders of magnitude for their interference to be significant [Sko03].

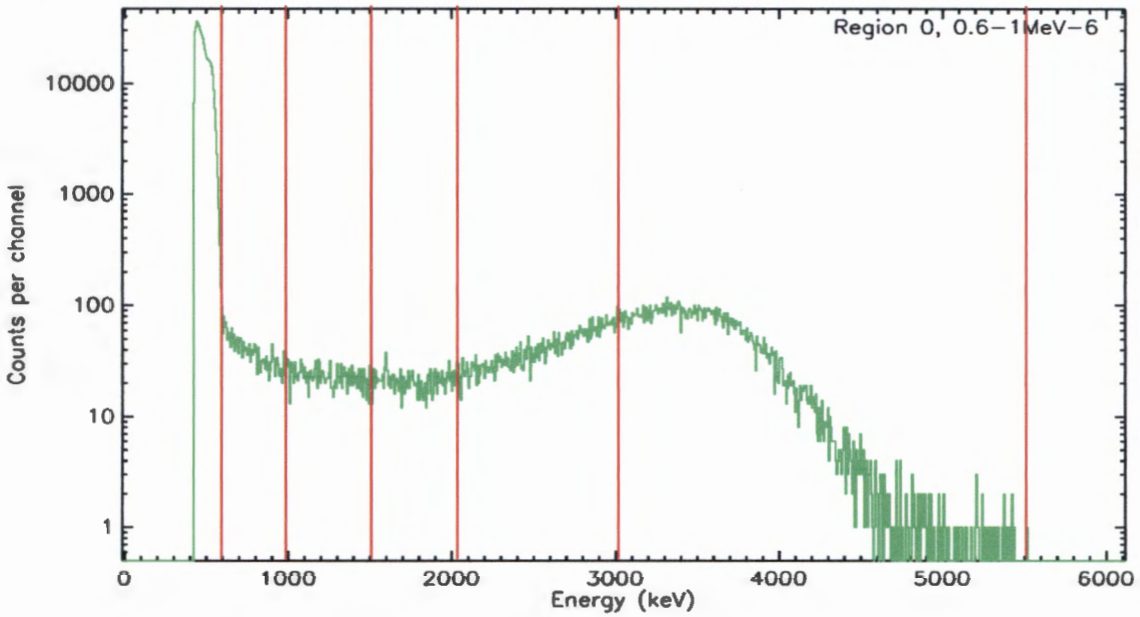

Fig.4.9 Particle energy spectrum from the SBD obtained with a boron standard. The 3 to 5.5MeV spectral region is used for quantitative B analysis.

The lower part of the spectrum (below 3000keV) won't be considered because as shown from the plate glass spectrum (fig 4.12) a lot of the alpha particles counted are from oxygen in that region. The idea is to obtain only counts from resultant 3 alphas of energy range above 3000 keV. From the above spectrum there is a clear accumulation of counts which shows that indeed there were some alphas detected although identification (of alphas) will be difficult as there is no clear peak of α_1 (should be 3.63 MeV at 172^0 Mon92). In the spectrum below there is a clear α_0 peak although it doesn't appear clearly in figure 4.9. The difference between the two spectra (figures 4.9 and 4.10) is because of the time spent in the collection of counts during the experiment. Though the α_0 is less

interesting due to less sensitivity, it can be more convenient to use for depth profiling at higher incident proton energy as it is well isolated from other alphas [Mon92].

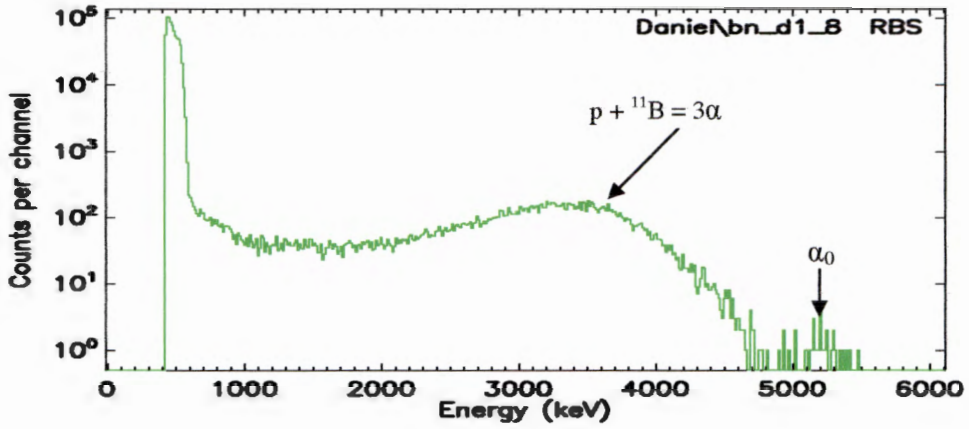

Fig 4.10: Glass 2 spectrum showing an α_0 peak

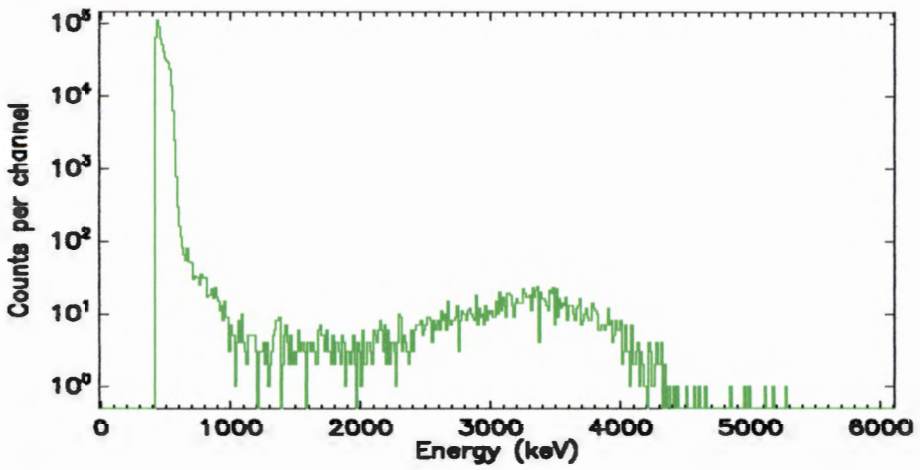

Fig 4.11: Glass 5 spectrum

The spectrum above (figure 4.11) shows less counts as expected because it comes from the glass with the lowest amount of boron. All of the above-shown spectra are from the proton backscattering with no subtracted background provided by the plate glass. From these spectra, depending on the resultant curve, the obtained yield will be used to calibrate for unknowns. There was measurement of plate glass under similar conditions to setup the energy window without the influence of oxygen (figure 4.12).

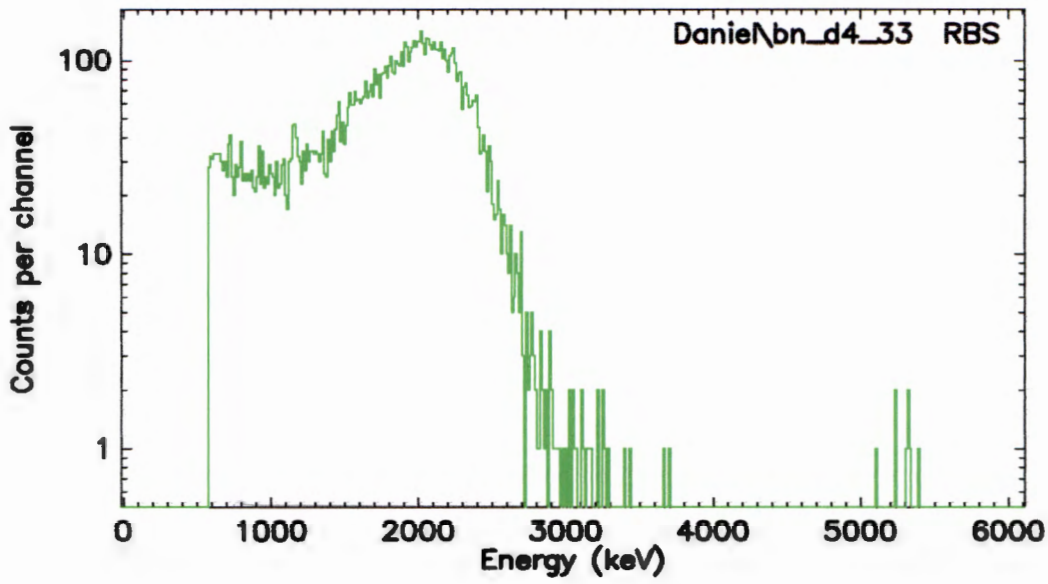

Fig.4.12 Plate glass spectrum

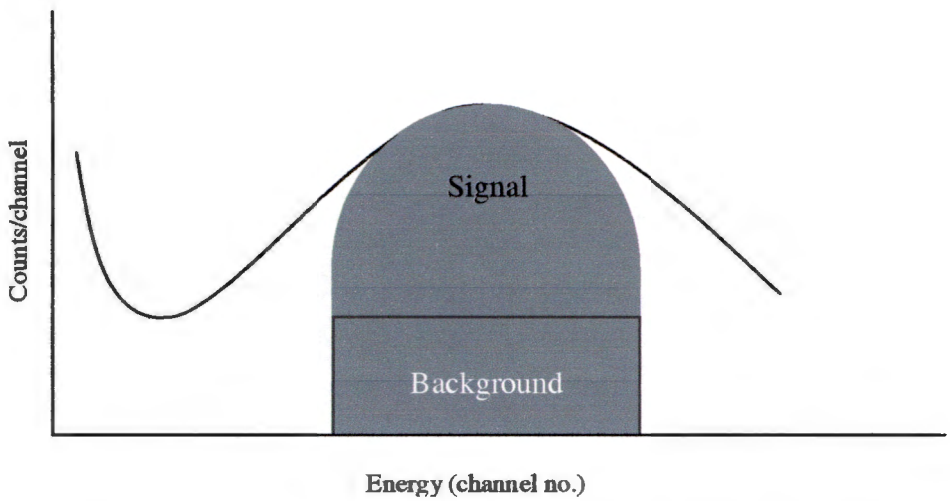

Fig.4.13 Anticipated charged particle spectrum
[Skogby, *et.al* , 2003]

From the above description to attain the final concentration of the unknowns we use the formula

$$\text{Concentration}_{(\text{unknown})} = \text{concentration}_{(\text{standard})} \times \frac{\left[\left(\frac{\text{signal}_{(\text{unknown})}}{\text{charge}_{(\text{unknown})}}\right) - \left(\frac{\text{background}}{\text{charge}}\right)\right]}{\left[\left(\frac{\text{signal}_{(\text{standard})}}{\text{charge}_{(\text{standard})}}\right) - \left(\frac{\text{background}}{\text{charge}}\right)\right]} \quad \text{Eq 4.1}$$

where the background is the counts from the plate glass sample. The lower energy window of the displayed spectrum (Fig.4.13) is going to be rejected

Table 4.7 EMP and B acquisition data (NRA using a-SBD) from a demarcated boron region

Mineral	B_2O_3 conc. (wt %)	Boron yield (counts/μC)
Glass-1	9.52[a]	232±0.89
Glass-2	7.97[a]	161±1.523
Glass-3	4.7[a]	124±1.56
Glass-4	1.99[a]	88±1.326
Glass-5	0.629[a]	46±0.753
BN	44.3[c]	75518±0.623
Tourmaline	10.54[b]	256±2.89

[a] Recalculated values from EMP chemical composition;
[b] Obtained from reference [Sko03]; [c] Obtained from EMP

Table 4.8 Boron concentration (in ppm) and acquisition data (NRA using a-SBD) from a demarcated boron region

Mineral	Boron conc. (ppm)	Boron yield (counts/μC)
NIST 612	(32)[d]	12±3.52
NIST 614	(1.3)[d]	9±11.203

[d] Uncertified values in mg/kg [www7]

Below are the BN maps corresponding to the BN values in table 4.7.

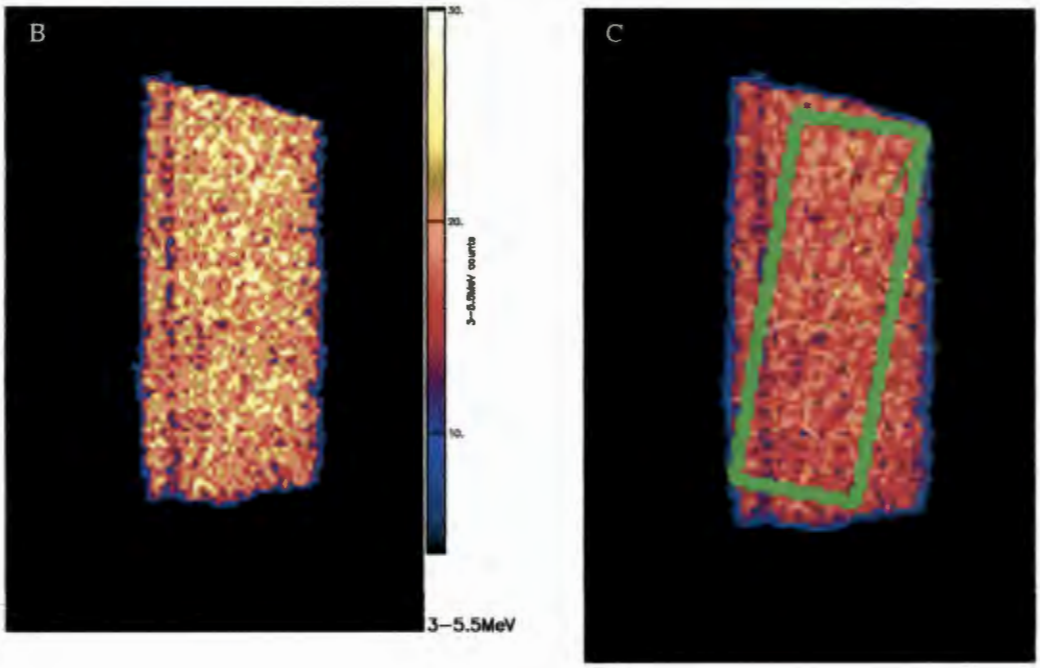

Fig 4.14 BN map displayed as counts (B) and its analyzed area (C), using a-SBD only.

4.4 NRA results using PIN photodiodes with Al foil.

The distortion seen on the energy calibrating spectra (figure 4.15) proved that it was always going to be difficult to attain correct data using the Al foil as the absorber.

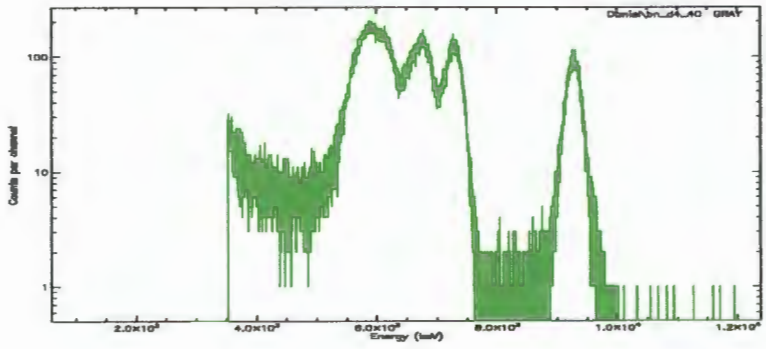

Fig 4.15 Thorium source spectra quad PIN photodiodes with Al foil

The distortion is attributed to the presence of the Al foil because for spectrum obtained without the presence of an absorber (figure 4.15); better resolutions were achieved (table 4.6). With such conclusion, the onus was to get the characteristics of the foil with the focus on cross-sections as the thickness had already being dealt with (page 45).

4.5 NRA results using PIN photodiodes without absorber

The obtained results from the previous data were not conclusive and also due to the bad resolution displayed when Al foil is used, leading to bad calibration, it was only good to look at using the diodes without an absorber and an effect was noticed when an energy calibrating spectrum was obtained from a Th-228 source as better resolution was observed (fig 4.15). This obviously meant better estimation of best minimum detection limits as the calibration would be improved though not to the most ideal level. The boron analyses results of this part (absorber-less PIN diodes) are summarized in table 4.8. The data presented include relevant measured raw data as well as the derived B concentration for our samples. The most positive thing before anything else was the fact that the glasses' boron weight values were corrected and this allowed for a better calibration curve for the 5 glasses that proved to be positive as the least-square fit ($r^2 \sim 1$) showed correlation which will allow for a straight line to pass through $y = x = 0$ (Fig 4.22). Using the same self equation 3.1, the results obtained were positive.

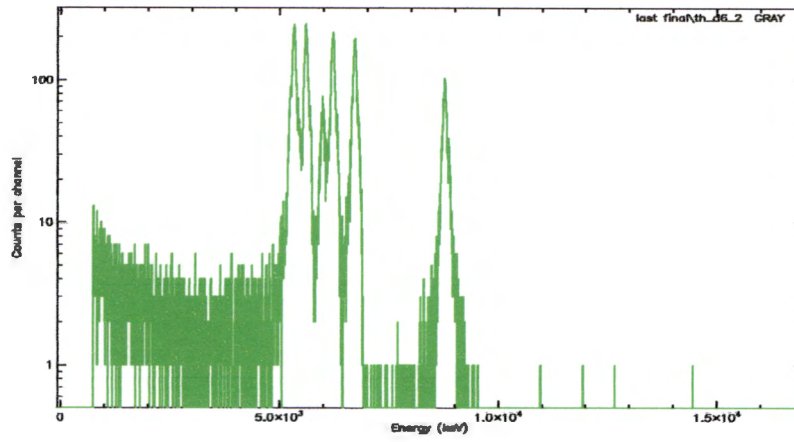

Fig 4.16 Thorium source spectra of quad PIN photodiodes without Al foil

The concern was then to see if the collected data spectrum would display a huge background due to backscattered protons. The acquired spectra displayed what was expected and that was due to the fine tuning of the lower level discriminator so as to avoid much flooding of the detector by backscattered protons. The resultant spectra proved to be precisely what was hoped for as a lot of them showed less background collection (e.g. fig 4.16). The maps acquired from the data collection done by PIN photodiodes showed a better resolution (see table 4.6) confirming the fact that a lot of the alpha particles were detected by them compared to the a-SBD. Some of the maps obtained are shown below with clear difference in intensity levels.

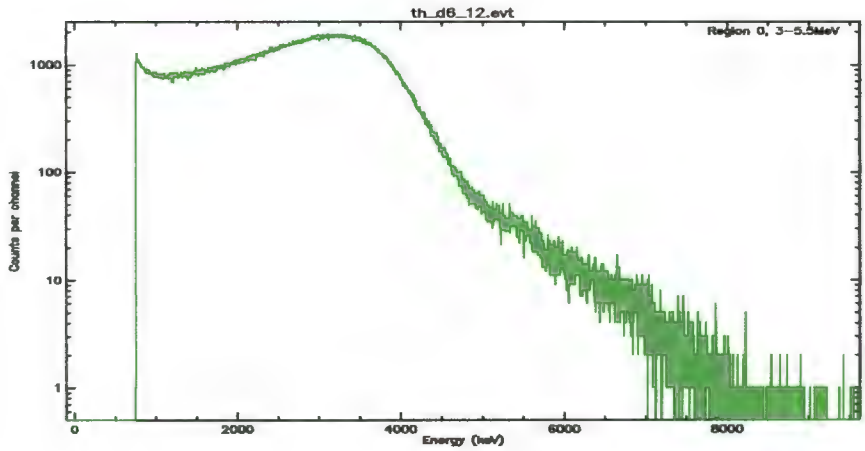

Fig 4.17 BN spectra from PIN photodiodes detector without absorber

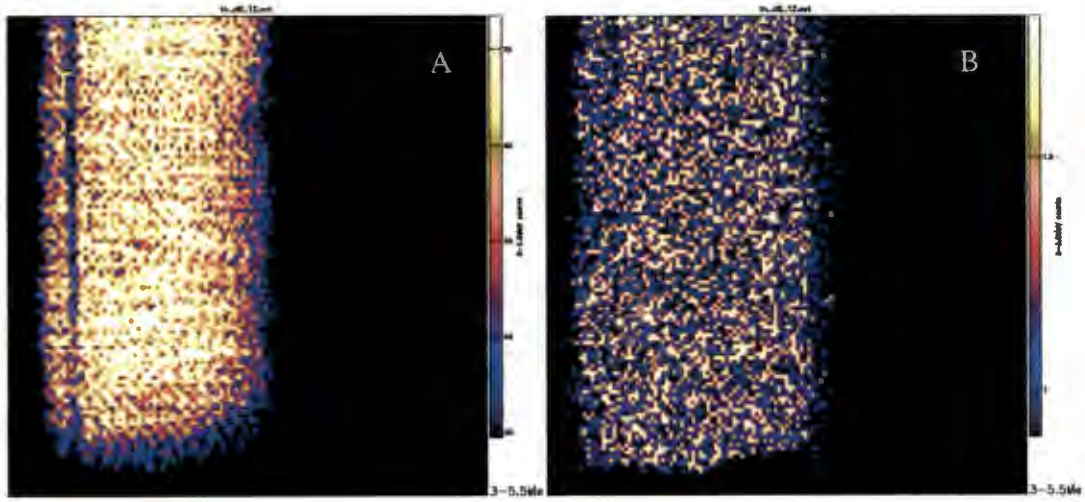

Fig 4.18 BN maps obtained from data by (a) PIN photodiodes and (b) a-SBD

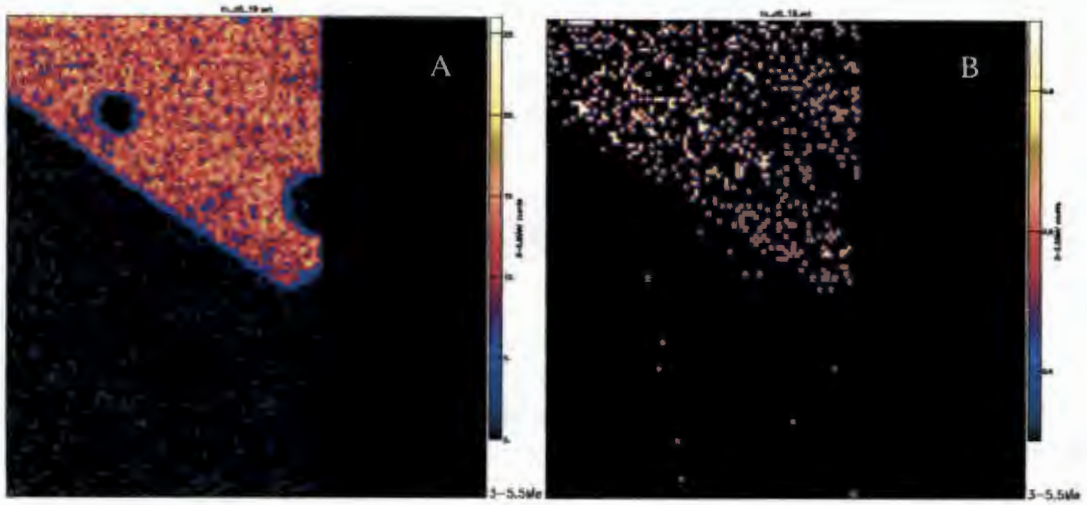

Fig 4.19 Glass 2 maps obtained from data by (a) PIN photodiodes and (b) a-SBD

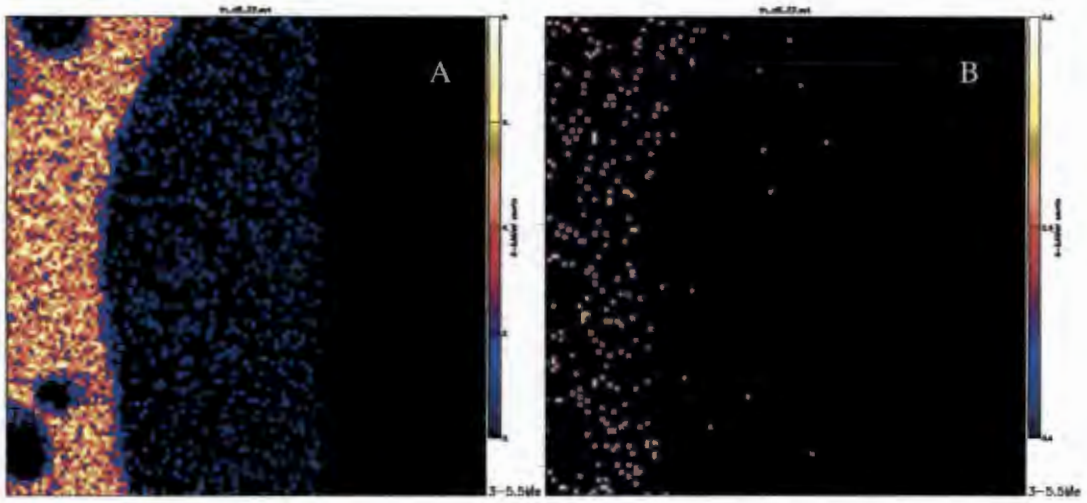

Fig 4.20 Glass 5 maps obtained from data by (a) PIN photodiodes and (b) a-SBD

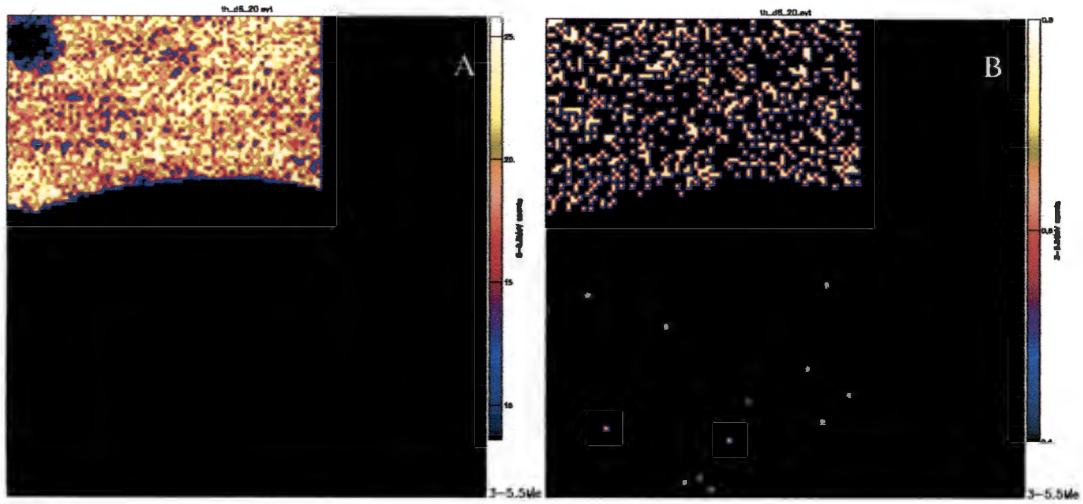

Fig 4.21 Glass 3 maps obtained from data by (a) PIN photodiodes and (b) a-SBD

Table 4.9 Counting statistics of the two detectors.

Mineral	PIN diodes counting statistics	a-SBD counting statistics
Glass-1	2213803	3979
Glass-2	1050111	2679
Glass-3	702524.3	1705
Glass-4	269783.5	410
Glass-5	254295.3	84
BN	33716790.95	65 425
Tourmaline	3179772.583	29908
NIST 612	1380.87	104
NIST 614	593.38	74

PIN diodes predictably showed better counting statistics, illustrated qualitatively in figures 4.18-4.21. The lack of counts on the annular-SBD can be attributed to the geometry inside of the chamber because for figure 4.14, when only annular-SBD was

used, the intensity of the map clearly shows that a lot of counts were obtained. With lack of counts for the pBS detector, the ideal data from table 4.10 was applied in pursuit of a calibration curve that will incorporate both counts.μC^{-1} of B_2O_3 weight percentages and boron elemental abundance (in ppm) from the standards {NIST 612, NIST 614 (in ppm), table 4.11} i.e. Boron concentration (ppm) versus counts.μC^{-1} were the counts of the samples will be used to extrapolate their Boron concentration in ppm. The results obviously depended on the calibration curve having the most possible least-square fit, ideally $r^2 = 1$ which will really mean the obtained MDL for certain counts is correct.

Table 4.10 Nuclear microprobe data of PIN photodiodes without absorber

Mineral	Calculated B_2O_3 conc. (wt %)	B conc. (ppm)	Boron yield (counts/μC)
Glass-1	9.52[a]	38384.64[d]	2213802±0.737
Glass-2	7.97[a]	32135.04[d]	1050111±1.342
Glass-3	4.7[a]	18950.4[d]	702524±1.312
Glass-4	1.99[a]	8023.68[d]	269783±1.219
Glass-5	0.629[a]	2536.128[d]	254295±0.809
BN	44.3[c]	435500[d]	33716791±0.562
Tourmaline	10.54[b]	42336[d]	3179773±3.174

[a] Recalculated values from EMP chemical composition;
[b] Obtained from reference [Sko03]; [c] Obtained from EMP;
[d] B concentration converted from wt% to ppm

Table 4.11 Boron concentration (in ppm) and acquisition data (PIN photodiodes without absorber) from a demarcated boron region

Mineral	Boron conc. (ppm)	Boron yield (counts/μC)
NIST 612	(32)[e]	1380±4.652
NIST 614	(1.3)[e]	593±10.685

[e] Uncertified values in mg/kg [www7]

Table 4.12 Obtained B_2O_3 concentrations (in wt %)

Mineral	[a] Calc. B_2O_3 conc. (wt %)	[b] EDS B_2O_3 conc. (wt %)	[c] Corr. B_2O_3 conc. (wt %)
Glass-1	9.52	23.7	27.23
Glass-2	7.97	17.9	12.775
Glass-3	4.7	16.5	8.456
Glass-4	1.99	14.0	3.079
Glass-5	0.629	9.7	2.886

[a] Concentrations obtained by calculations after sample preparation
[b] Concentrations obtained from EDS analysis
[c] Concentrations obtained through the use of Eq 3.1(background subtracted)

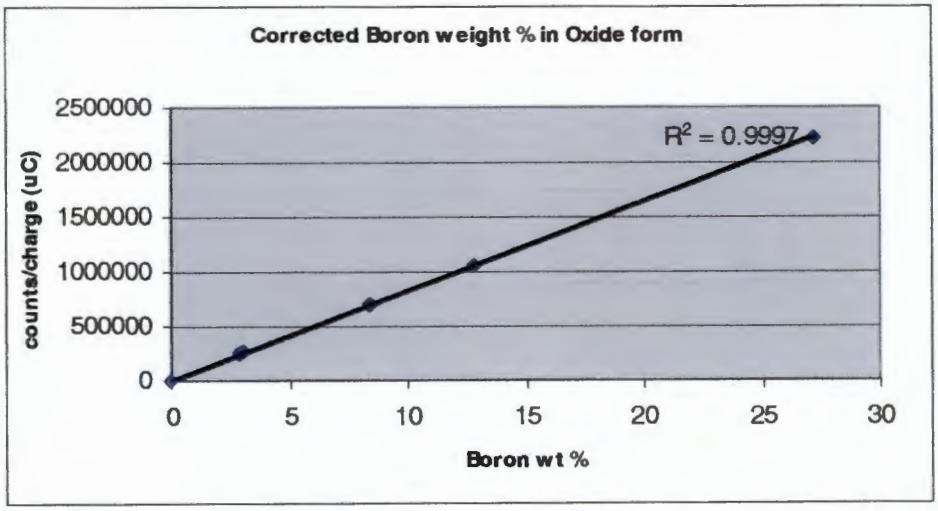

Fig 4.22 Calibration curve displaying NMP data acquired through PIN diodes without absorber

The above calibration curve (Fig 4.22) shows a good linear graph because both the background subtracted and the concentrations of the boron oxide were constant for all the glasses. The most interesting factor was the linearity of the curve as proved by the least square fit (r^2) value. The only disturbing factor was the boron content as it was in an oxide form rather than in elemental abundances. Obviously it was ideal to just convert the B_2O_3 into boron elemental abundances (ppm) to achieve the main aspect of the whole study, with the hope of getting a similar calibration curve. From the conversion, the obtained concentration didn't correlate perfectly with their yield (fig. 4.23) as in the figure 4.22. That can be attributed to the fact that the concentration values were from the EDS (table 4.4) which as explained before is not a good trace elements profiling technique and also the unsubtracted background. A better correlation was obtained when B_2O_3 values from table 4.10 were converted to boron elemental abundances (ppm) and used (fig 4.24).

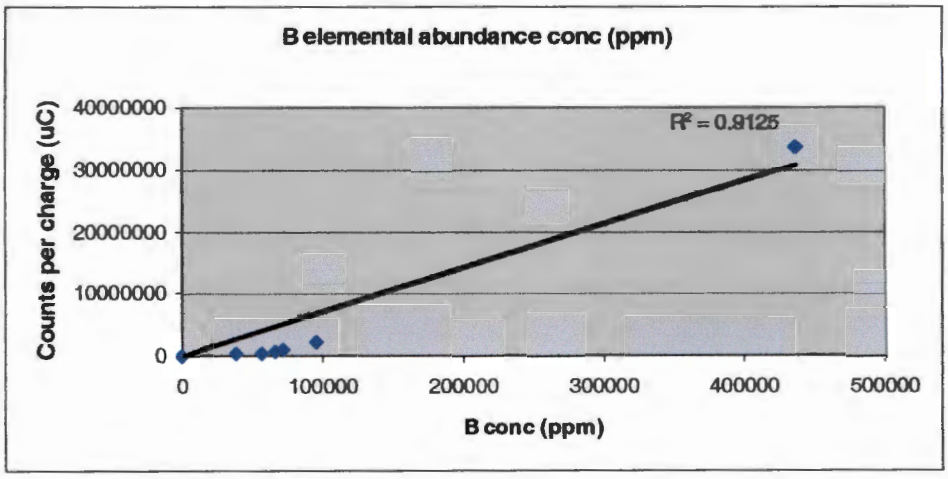

Fig 4.23 Uncorrected EDS Boron concentration values (ppm)

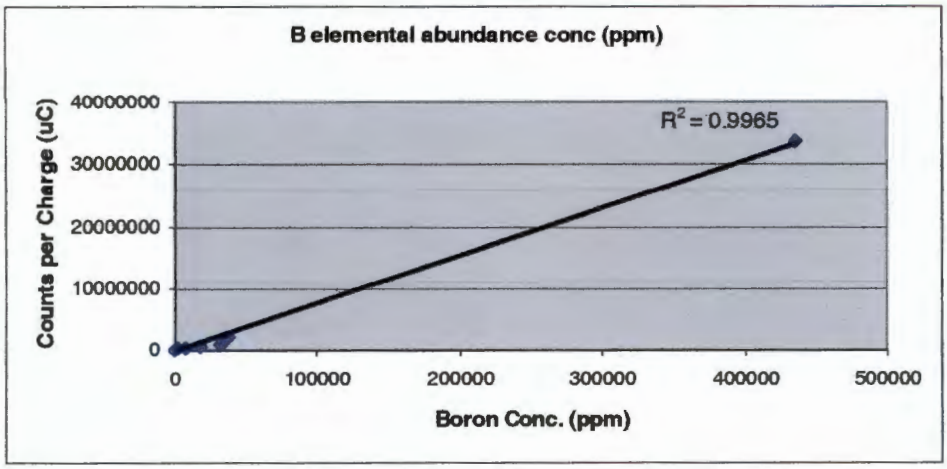

Fig 4.24 Uncorrected calculated Boron concentration values (ppm)

With the two curves showing discrepancies relative to the trendline, both sets of concentration values were applied on the same set of axes to see their difference with respect to true values, ie. along the trendline (fig 4.25). It can be clearly seen that the calculated boron values (table 4.10) in ppm showed better correlation. The inclusion of the EDS values though is important because a conclusion on the correct concentration values couldn't be taken on a single set without comparison.

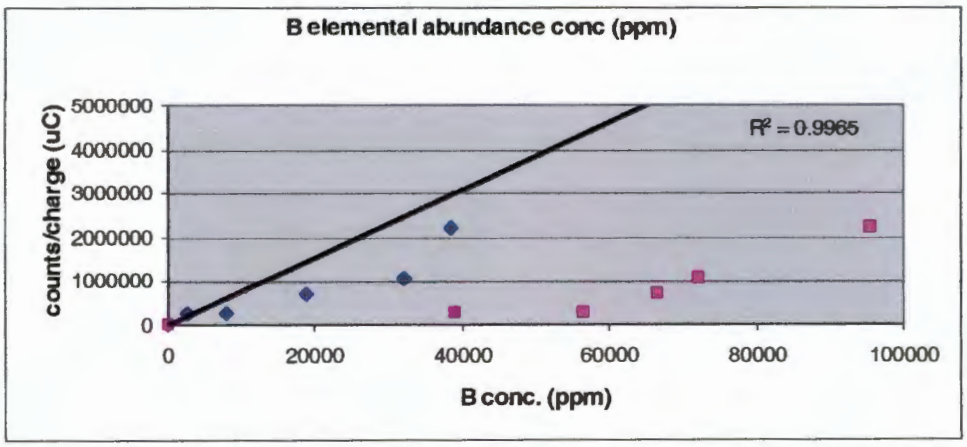

Fig 4.25 Uncorrected calculated (blue) and EDS (pink) Boron concentration values (ppm)

Both sets of Boron concentrations, figure 4.25, show their difference relative to the linear trend with the EDS values showing bigger error margins. That can possibly be attributed

to electron loss during the EMP experiment as compared to the counts obtained from the NMP experiment. Due to poor linearity, glasses were removed and only NIST 612, NIST 614, tourmaline and BN data from tables 4.10 and 4.11 was used. Charge normalization was used as there was clear evidence of little or no background. From figure 4.25, the least square fit (r^2) value does show the unreliability of the glasses because when omitted, a perfect linear graph is obtained. The error bars (1σ) in the graphs were based on counting statistics with error percentage of 5. The standards (NIST 612, NIST 614, tourmaline and BN) concentration show good correlation to the normalized counts. This shows that they can be used as calibrating standards for some unknowns with perceived low boron concentration. The standards would be good for compounds that show negligible background as the all of the above were taken from spectra with very low background as depicted by the plate glass spectra (Fig.4.12) hence no correction (background subtraction) was done. This is because provided all the precautions are considered, $^{11}B(p,\alpha)\ ^{8}Be$ reaction gives high-energy alpha particles that can be detected almost background free [Kri99].

For the glasses, both the results of calculations and EDS results are not reliable and NRA with PIN diodes proves that. Only from NRA can we obtain the new results which are correct. So in the future these glasses can be used but with concentration values as found from NRA. The MDL values (see appendix) were obtained in B elemental form relative to their accumulated charge.

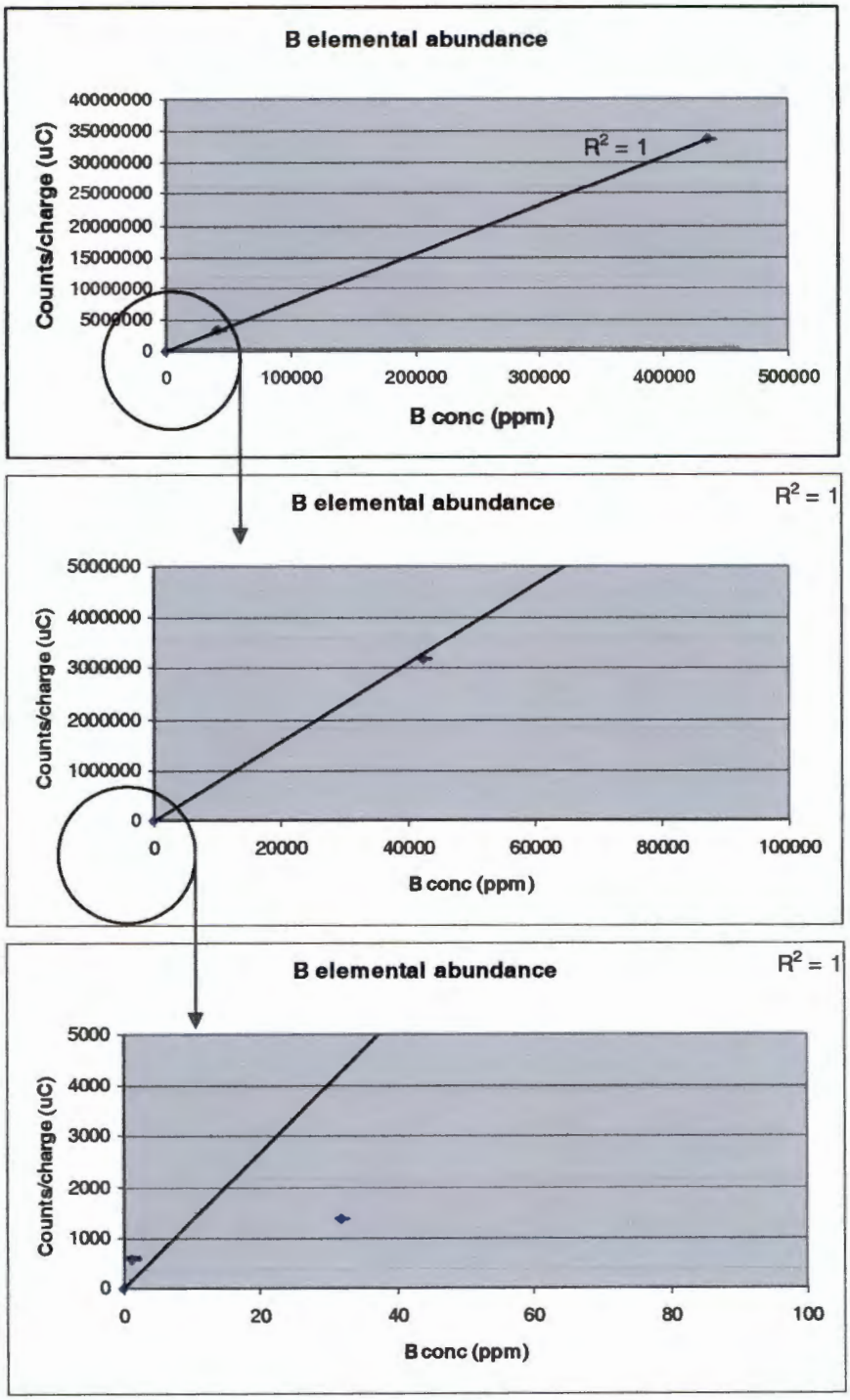

Fig 4.26 Boron standards concentration values (ppm)

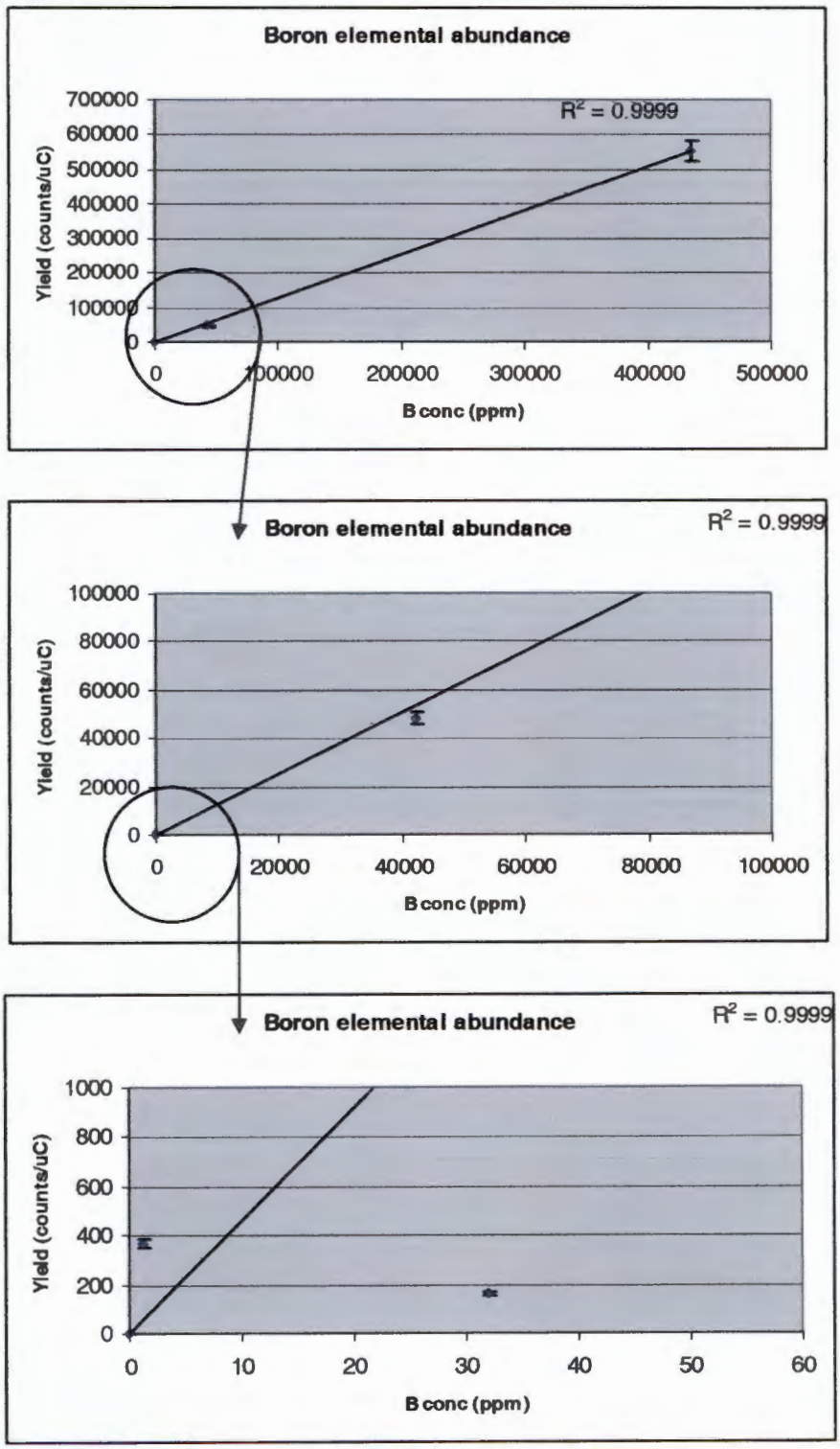

Fig 4.27 Boron standards concentration values (ppm) obtained from a-SBD counts in the presence of PIN diodes

Chapter 5

5.1 Summary

The study's main objective was to find the lowest possible boron minimum detection limits using the nuclear reaction, $^{11}B(p,\alpha)\ ^{8}Be$, (see appendix) and the large area PIN photodiodes. The analytical techniques EDS, SEM and NRA were applied were physically prepared glasses and standards were investigated. A computer simulation of the RBS spectrum was done using RUMP. Other computer soft wares applied during data analysis included INCA, SRIM and Geo-PIXE.

The photodiodes showed spectra with lot of distortions when used with an Al foil but less background and much improved detector resolution was seen when there was no absorber used. Further investigation led to conclusion that the absorber itself has an effect on the background. The most exciting feature was spectra obtained with no absorber as all of them showed less or no background. Glass boron concentrations determined by EDS and those that were calculated are not comparable and are both not reliable to be used as calibrating standards. This is because of their sparse distribution relative to the linear trend. The contributing factors for the observed flaws can be they were not homogeneous, uneven grinding and faulty weighing during preparation. It would be very wise to have a standard of well known B_2O_3 weight concentration so that it can be used during calibration especially if stopping-power α-yield corrections have been done. This will help as good correlation will be achieved because only a single boron standard will be adequate for calibration [Sko03]. Even from the EMP, it would be advisable to have a standard of proven concentration so as to have correct weight percentages before a correct calibration can be achieved.

With the new array of detectors the boron MDL value was decreased to 1.3μg/g which is the concentration for NIST 614 for 0.303μC accumulated charge. The NIST standards proved the study conditions to be good because their counts shows that very low detection limits can be achieved. The least square fit (r^2) in figure 4.27 showed the reliability offered by the standards (tourmaline and BN) with the tourmaline presenting good positioning on the linear trend as its values (coordinates) were vital for calibration. The NIST standards show bad positioning relative to the linear trend but as mentioned the positive result is the fact that they can be identified though they have very low concentrations.

5.2 Conclusions

- The study showed that EMP cannot detect boron at levels below 10 weight percent.
- The errors obtained were done only for the yield because the boron weight percentages were taken as absolute values for both EDS and calculated values.
- Although there was some background, the PIN photodiodes proved to be able to achieve better counts which mean a lot of α-particles were being collected even for low boron content samples.
- The resolution of the PIN photodiodes was much better when an absorber was not used because there is lack of Al cross-section at high energies.
- Charge measurements were good as shown by the yield obtained for both tourmaline and BN, and that is credited to capabilities of the beam on-demand deflection systems.

5.3 Recommendations

- The Geo-PIXE software showed many unexpected problems when making use of counts collected from selected energy windows, which is a necessity in NRA analysis.
- Standards with precisely known boron concentration (ppm) to be used when calibrating for determination of unknowns.
- Try minimizing the noise (light) by covering any exposure to the diodes by a dark, light absorbing material because the diodes are very sensitive.

LIST OF FIGURES AND TABLES

LIST OF FIGURES

LABEL		PAGE
[Fig.2.1]	Types of ion beam techniques possible at the iThemba Labs NMP	4
[Fig.2.2]	Laboratory and centre-of-mass reference coordinate systems	5
[Fig.2.3]	Experimental layout demonstrating the concept of differential scattering cross section	6
[Fig.2.4]	Backscattering events in a sample consisting of a monoisotopic element	9
[Fig.2.5]	Illustration of different NRA reaction types	15
[Fig.2.6]	Liquid scintillator spectrum of neutrons of two different energies	17
[Fig.2.7]	Characteristic NRA experiment geometry	19
[Fig.2.8]	A schematic view of RBS analysis	25
[Fig.2.9]	Illustration of an elastic collision between incident ion and a target mass	28
[Fig.2.10]	Schematic diagram of a SIMS process	29
[Fig 2.11]	Scanning Electron Microscope Setup	31
[Fig 2.12]	The Schematic Illustration of SEM Process	32
[Fig 2.13]	Possible nuclear reactions of protons and ^{11}B	35
[Fig.3.1]	Depiction of the Van de Graaff accelerator and NMP layout at iThemba Labs.	39
[Fig.3.2]	The inside of the MRG NMP Chamber	41
[Fig.3.3]	Si PIN photodiodes detector at MRG NMP Chamber, iThemba LABS	43
[Fig.3.4]	Al foil RUMP simulation	45
[Fig.3.5]	Velocity diagram for nuclear reaction $^{11}B(p,\alpha)\ ^{8}Be^{*}$	46
[Fig.3.6]	Angles covered by the Si PIN photodiodes at NMP, MRG	46
[Fig.4.1]	Optical micrograph of glass 1	49
[Fig.4.2]	SEM structural map of glass 1	50

[Fig.4.3] SEM spectra of BN.....51

[Fig.4.4] SEM spectra of glass 1.....52

[Fig.4.5] Thorium source spectra of single diode without an Al foil.....57

[Fig. 4.6] Thorium source spectra of single diode with Al foil.....58

[Fig.4.7] The figure showing the position of boron at Ep = 700 keV.....59

[Fig.4.8] A Nuclear Microprobe Chamber with mounted Si PIN photodiodes.....61

[Fig.4.9] Particle energy spectrum from the SBD obtained with a boron standard.....62

[Fig. 4.10] Glass 2 spectrum showing an α_0 peak.....63

[Fig 4.11] Glass 5 spectrum.....64

[Fig 4.12] Plate glass spectrum.....65

[Fig 4.13] Anticipated charged particle spectrum.....66

[Fig 4.14] BN map displayed as counts and its analyzed area, using a-SBD only.....68

[Fig 4.15] Thorium source spectra quad PIN photodiodes with Al foil.....68

[Fig 4.16] Thorium source spectra quad PIN photodiodes without Al foil.....70

[Fig 4.17] BN spectra from PIN photodiodes detector without absorber.....71

[Fig 4.18] BN maps obtained from data by PIN photodiodes and a-SBD.....71

[Fig 4.19] Glass 2 maps obtained from data by PIN photodiodes and a-SBD.....72

[Fig 4.20] Glass 5 maps obtained from data by PIN photodiodes and a-SBD.....72

[Fig 4.21] Glass 3 maps obtained from data by PIN photodiodes and a-SBD.....73

[Fig 4.22]Calibration curve displaying data acquired through PIN diodes without absorber.75

[Fig 4.23] Uncorrected EDS Boron concentration values.....76

[Fig 4.24] Uncorrected calculated Boron concentration values.....77

[Fig 4.25] Uncorrected calculated final and EDS Boron concentration values.....77

[Fig 4.26] Boron standards concentration values (ppm).....79

[Fig 4.27]Boron standards concentration values (ppm) obtained from a-SBD counts in the presence of PIN diodes 80

LIST OF TABLES

Table 2.1 Comparison of different STIM analysis ions.....22

Table 2.2 Nuclear microprobe analyses compared with other techniques.....33

Table 3.1 Al foil Stopping Range of Ions in Materials (SRIM) Calculations.....44

Table 3.2 Al foil Stopping Range of Ions in Materials (SRIM) Calculations.....47

Table 4.1 Chemical composition and weight of B_2O_3 weight %.....52

Table 4.2 Elemental abundances in weight percentages real values.....53

Table 4.3 Elemental abundances in weight percentages (normalized data).....54

Table 4.4 Al, Si and K real values.....55

Table 4.5 Recalculated and normalized Boron values.....55

Table 4.6 Resolutions obtained for different PIN diode conditions.....59

Table 4.7 EMP and B acquisition data from a demarcated boron region.....67

Table 4.8 Boron concentration and acquisition data from a demarcated boron region.67

Table 4.9 Counting statistics of the two detectors.....73

Table 4.10 PIN photodiodes nuclear microprobe data without absorber.....74

Table 4.11Boron concentration and acquisition data from a demarcated boron region.75

Table 4.12 Obtained B_2O_3 concentrations (in wt %).....75

APPENDIX

Calculations of Al foil thickness in micrometers

From the simulation:

$$\text{Thickness [g/cm2]} = \frac{\text{Thickness (from rump)} \times \text{mass/ \# of atoms}}{\text{Avogadro's constant}}$$

$$= \frac{65300\text{e}15 \text{ at/cm2} \times 26.98 \text{ g/mol}}{6.022\text{e}23 \text{ at/mol}}$$

$$= 0.0029 \text{ g/cm}^2$$

$$\text{Thickness [}\mu\text{m]} = \frac{\text{Thickness (g/cm}^2\text{)}}{\text{Density (g/cm}^3\text{)}}$$

$$= \frac{0.0029 \text{ g/cm}^2}{2.7 \text{ g/cm}^3}$$

$$= 0.00107\text{cm}$$

$$= 0.0000107\text{m}$$

$$= 10.74 \text{ }\mu\text{m}$$

From the measured and weighed Al foil values:

$$\text{Volume (cm3)} = \frac{\text{Mass (g)}}{\text{Density (g/cm}^3\text{)}}$$

$$= \frac{0.308 \text{ g}}{2.7 \text{ g/cm}^3}$$

$$= 0.114 \text{ cm}^3$$

$$\text{Thickness [µm]} = \frac{\text{Volume (cm}^3\text{)}}{\text{Area (cm}^2\text{)}}$$

$$= \frac{0.114\ \text{cm3}}{100\ \text{cm}^2}$$

$$= 0.0000114\ \text{m}$$

$$= 11.4\mu\text{m}$$

From the values of the publication [Szi04]

$$\text{Thickness [µm]} = \frac{\text{Thickness (g/cm}^2\text{)}}{\text{Density (g/cm}^3\text{)}}$$

$$= \frac{2.5\ \text{mg/cm}^2}{2.7\ \text{g/cm}^3}$$

$$= \frac{2.5\text{e-}3\ \text{g/cm}^2}{2.7\ \text{g/cm}^3}$$

$$= 0.000925\ \text{cm}$$

$$= 0.00000925\ \text{m}$$

$$= 9.26\ \mu\text{m}$$

Mineral	Counts/charge (uC)	Calculated B conc. (ppm)	EDS conc(ppm)	Error
BN	435500	33716790.95	435500	0.562894883
Glass 1	38384.64	2213803	95558.4	0.737929676
Glass 2	32135.04	1050111	72172.8	1.342357344
Tourmaline	42336	3179772.583	42336	3.174335546
Glass 3	18950.4	702524.3	66528	1.312206717
Glass 4	8023.68	269783.5	56448	1.219465796
Glass 5	2536.128	254295.3	39110.4	0.809217411
NIST 612	32	1380.87	32	4.652153465
NIST 614	1.3	593.38	1.3	10.68579399

Minerals, Yield, B concentrations and errors used in figures 4.24 and 4.25

Aluminium SRIM Calculations			
Ion Energy (keV)	dE/dx(Electronic)	dE/dx(Nuclear)	Projected range(um)
650.00	2.20×10^{-02}	1.81×10^{-01}	7.77
660.00	2.18×10^{-02}	1.79×10^{-01}	7.93
670.00	2.16×10^{-02}	1.76×10^{-01}	8.1
675.00	2.16×10^{-02}	1.75×10^{-01}	8.19
680.00	$2.\times10^{-02}$	1.74×10^{-01}	8.27
690.00	2.13×10^{-02}	1.72×10^{-01}	8.44
700.00	2.12×10^{-02}	1.70×10^{-01}	8.62

Al foil Stopping Range of Ions in Materials (SRIM) Calculations

Aluminium SRIM Calculations			
Ion Energy (MeV)	dE/dx(Electronic)	dE/dx(Nuclear)	Projected range(mm)
5.3405	4.99	1.82×10^{-03}	61.38
5.4233	4.93	1.79×10^{-03}	63.05
5.6856	4.78	1.72×10^{-03}	68.45
6.0510	4.57	1.62×10^{-03}	76.26
6.2883	4.46	1.56×10^{-03}	81.51
6.7785	4.24	1.46×10^{-03}	92.79
8.7840	3.59	1.15×10^{-03}	144.43

Al foil Stopping Range of Ions in Materials (SRIM) Calculations

Detailed procedure

Add SiO_2, Al_2O_3 and K_2CO_3 then grind. Make paste using acetone. Divide the base into 5 equal parts then multiply one sample part with a corresponding B_2O_3 percentage and the product will be the amount of the B_2O_3 needed (eg, part 1 × B_2O_3% = amount of B_2O_3 needed). After dividing the parts, add B_2O_3 grind, fire at 900^0C where K_2CO_3 dissociates to K_2O as CO_2 is given off. After placing the glasses on the epoxy, thickening, drying and labeling, then follows the polishing.

Polishing

Take the labeled resin and scrub on the 400- initially then the 1000-labelled sandpaper with the water flowing, then on the polishing machine, lubricate both the resin and the polishing machine with a paste then use it to 250 revolutions/second speed. Place and hold the resin for ~ 10 minutes whilst the machine is rotating. Rinse the resin and then check the positions of your glasses under the microscope for better numbering.

Different resolutions observed using Th-228 source

Complete diodes without absorber

Energy (MeV)	Channel	FWHM (channels)	FWHM (KeV)
5.42333	1347.7	39.1	160.64
5.68556	1417.4	29.08	119.47
6.28829	1561.2	31.55	129.62
6.7785	1677.4	35.6	146.26
8.78437	2165.8	49.01	201.35

Complete diodes with absorber

Energy (MeV)	Channel	FWHM (channels)	FWHM (KeV)
5.42333	1599.5	48.53	167.02
5.68556	1683.2	36.26	124.79
6.28829	1856.6	40.47	139.28
6.7785	1991.8	48.79	167.91
8.78437	2576.1	78.87	271.43

Using a-SBD

Energy (MeV)	Channel	FWHM (channels)	FWHM (KeV)
5.34054	274.7	1.96	39.61
5.42333	279	2.23	45.07
5.68556	292	2.79	56.39
6.28829	322.3	2.68	54.16
6.7785	346.7	3.03	61.24
8.78437	445.3	4.62	93.37

MDL values for the standards

Standard	MDL (μg/g)	Accumulated charge (μC)
BN	435500	0.253
Tourmaline	42336	1.003
NIST 612	32	1.012
NIST614	1.3	0.303

REFERENCES

[And97] Andersen H.H. and Ziegler J.F., Hydrogen stopping powers and ranges in all elements. Vol. 3 (Pergamon press, New York, 1997) 2,3,12

[Bar99] Barradas N.P. and Smith R., Simulated annealing analysis of nuclear reaction analysis measurements of polystyrene systems. Jour. Phys. D: Appl. Phys. 32 (1999) 2964-2971

[Bei95] Beiser Arthur, Concepts of modern physics. 5th Edition. (1995)

[Bre96] Breese Mark B.H., Jameson David N., Phillip King J.C., Materials analysis using a nuclear microprobe. (1996)

[Chi95] Changgeng Liao, Hui Jian, Yongqiang Wang, Zhiahao Zheng, Boron depth profiles in Silicon and simulation α-spectra layer. Nucl. Instr. And Meth. In Phys. Res B 95 (1995) 97-101

[Chi01] Chiari M., Guintini L., Mandò P.A., Taccetti N., Proton elastic scattering cross-section on boron from 0.5 to 3.3 MeV. Nucl. Instr. And Meth. In Phys. Res B 184 (2001) 309

[Chu78] Chu Wei-Kan, Mayer James W., Nicolet Marc-A., Backscattering spectrometry. (1978) 23-

[Dea57] Dearnaley G., Dissanaike G.A., French A.P., and Lindsay Jones G., Study of B^{11} + p reactions. Physical Review, Vol. 108, Number 3, November 1, 1957

[Dec78] Deconnick G., Introduction to radioanalytical physics. Nuclear Monographs 1 (1978) 16

[Dem95] Demortier G., Analysis of light elements with a nuclear microprobe – A review. Nucl. Instr. And Meth. In Phys. Res B 104 (1995) 244

[Doo86] Doolittle L.R. A semiautomatic algorithm for Rutherford backscattering analysis. Nucl. Instr. and Meth. in Phys. Res. B15 (1986) 227-231.

[Ele00] Elekes Z., Kiss Á., Biron I., Calligaro T., Salomon J., Thick targets γ-ray yields for light elements measured in the deuteron energy interval of 0.7 – 3.4 MeV. Nucl. Instr. And Meth. In Phys. Res B 168 (2000) 305

[Fel86] Feldman L. C., Mayer W. J., Fundamentals of surface and thin film analysis. (1986) 15, 288, 303

[Gol]Goldstein Joseph, Newbury Dale, Joy David, Lyman Charles, Echlin Patrick, Lifsin Eric, Saywer Linda, and Michael Joseph, Scanning Electron Microscopy and Microanalysis. 3rd edition 12-

[Gre96] Grew E. S., & Anovitz L. M., Boron. Mineralogy, Petrolohy and Geochemistry. Review in mineralogy. Vol. 33 (1996) 1

[Hål00] Hålenius U., Kristiansson P., Skogby H., Boron subtitution in diopside evaluated through ^{11}B nuclear reaction reaction analysis. Phys. Chem. Minerals (2000) 27:681-688

[Hua95] Huang M. B., Huang L. J., Mitchell I. V., Lennard W. N., Lau W. M., Nöel J. P., Boron depth profiling in a δ-doped Si layer. Nucl. Instr. And Meth. In Phys. Res B 100 (1995) 149-154

[Joh95] Johansson S. A. E., Campbell L. J., Malmqvist K. G., eds in; Particle Induced X-ray Emission Spectroscopy Vol 133. 1995 John Wiley & Sons, Inc.

[Kri99] Kristiansson P., Hålenius U., Skogby H., Elfman M., Malmqvist K., Pallon J., Boron distributions in single crystals investigated with nuclear rection microanalysis. Nucl. Instr. And Meth. In Phys. Res B 158 (1999) 562

[Lap85] Lappalainen R., Räisänen J., and Analysis of boron using the (p,α) reaction. Nucl. Instr. And Meth. In Phys. Res B 9 (1985) 55

[Liu02] Liu Jiarui., Lu Xinming., Wang Xuemei., Chu Wei-Kan., Cross-sections of $^{11}B(p,\alpha)^{8}Be$ reaction for boron analysis. Nucl. Instr. And Meth. In Phys. Res B 190 (2002) 107

[May98] Mayer M., Annen A., Jacob W., Grigull S., The $^{11}B(p,\alpha_0)^8Be$ nuclear reaction and $^{11}B(p,p)^{11}B$ backscattering cross-sections for analytical purposes. Nucl. Instr. And Meth. In Phys. Res B 143 (1998) 244

[Mic94] Michaud V., Toulhoat N., Trocellier P., Courel P., Elemental and isotopic distribution of boron and lithium in tourmalines using nuclear microprobe. Nucl. Instr. And Meth. In Phys. Res B 85 (1994) 881

[Mon92] Moncoffre N., Analysis of boron by charged particle bombardment. Nucl. Instr. And Meth. In Phys. Res B 66 (1992) 126

Moncoffre N., Millard N., Jaffrezic H., and Tousset J., Boron analysis of thin layers using prompt nuclear techniques. Nucl. Instr. And Meth. In Phys. Res B 45 (1990) 81

[Oli74] Olivier C., Pierce T. B., The determination of boron in steels by measurement of the alpha-particles emitted during charged-particle irradiation. Radiochemical, Radioanalytical Letters 17, /5-6/, 335-342,1974

[Pil92] Pillay A. E., and Peisach M., Some studies on nuclear methods for boron determination. Nucl. Instr. And Meth. In Phys. Res B 66 (1992) 226

[Pro95] Prozesky V., M., Przybylowicz W. J., van Achterbergh E., Churms C. L., Pineda C. A., Springhorn K. A., Pilcher J. V., Ryan C. G., Kritzinger J., Schmitt H., Swart T., The NAC nuclear microprobe facility. Nucl. Instr. And Meth. In Phys. Res B 104 (1995) 36

[Prz99] Przybylowicz W. J., Mesjasz-Przybylowicz J., Pineda C. A., Churms C. L., Springhorn K. A., and Prozesky V., M Biological applications of the NAC nuclear microprobe. X-ray Spec. 28 (1999) 237

[Ree92] Reed William P., National Institute of Standards and Technology, Certificate of Analysis: Standard Reference Materials, (January 27, 1992)

[Rio95] Rio S., Métrich N., Mosbah M., Massiot P., Lithium, boron and beryllium in volcanic glasses and minerals studied by nuclear microprobe. Nucl. Instr. And Meth In Phys. Res B 100 (1995) 141-148

[Sjö95] Sjöland K. A., Kritiansson P., Tallone P., Nuclear reaction analysis of boron for microbeam analysis of medical samples. Nucl. Instr. And Meth. In Phys. Res B 104 (1995) 255

[Sjö97] Sjöland K. A., Kritiansson P., Elfman M., Malmqvist K., Pallon J., Utui R.J., Yang C., The new nuclear reaction analysis facility at the Lund nuclear microprobe. Nucl. Instr. And Meth. In Phys. Res B 130 (1997) 20-24

[Sko03] Skogby Henrik, Kristiansson Per, and Hålenius Ulf., An assessment of nuclear microprobe analyses of B in silicate minerals. American Mineralogist Vol. 88 (2003) 1601

[Szi04] Sziki Gusztáv, Dobos Erik, Kertész Zsófia, Szikszai Zita, Uzonyi Imre, Kiss Árpád Zoltán, A PIN detector array for the determination of boron using nuclear reaction analysis at a microprobe. Nucl. Instr. And Meth. In Phys. Res B 219 (2004) 240

[Tes95] Tesmer Joseph R., Nastasi Michael, Handbook of modern ion beam materials. (1995) 142, 143

[Tro99] Trompetter W. J., Reyes A. G., Vickridge I. C., Markwitz A., Lithium and boron in geological samples. Nucl. Instr. And Meth. In Phys. Res B 158 (1999) 56

[Vol96] Vollmer M., Meyer J. D., R. Michelmann W., Bethge K., Boron detection using the nuclear reaction $^{11}B(p,\alpha)2\alpha$. Nucl. Instr. And Meth. In Phys. Res B 117 (1996) 21-25

[Wat87] Watt F. and Grime G.W.,eds in: Principles and applications of high-energy ion microbeams. (1987)

[Weg04] Wegdén M., Kritiansson P., Ceberg C., Munck af Rosenschöld P., Auzelyte V., Elfman M., Malmqvist K. G., Nilsson C., Pallon J., Shariff A., Nuclear microprobe analysis of the selective boron uptake obtained with BPA in brain tumour tissue. Nucl. Instr. And Meth. In Phys. Res B 219 (2004) 67

[Zie85] Ziegler J. F., Biersack J. P., and Littmark U., The stopping and range of ions in solids. Vol 1 (Pergamon press, New York, 1985) 14

[www1] http://people.ccmr.cornell.edu
[www2] http://www.ulg.ac.be
[www3] http://en.wikipedia.org
[www4] www.seagrant.sunysb.edu
[www5] http://www.lpdlabservices.co.uk
[www6] http://mse.iastate.edu
[www7] https://srmors.nist.gov
[www8] http://www2.arnes.si
[www9] http://www-nds.iaea.org
[www10] http://www.microbeams.co.uk